Monthly Notices
of the
ROYAL ASTRONOMICAL SOCIETY

MNRAS **477,** 153–174 (2018)
Advance Access publication 2018 March 14

doi:10.1093/mnras/sty632

On the type Ia supernovae 2007on and 2011iv: evidence for Chandrasekhar-mass explosions at the faint end of the luminosity–width relationship

C. Ashall,[1,2★] P. A. Mazzali,[2,3] M. D. Stritzinger,[4] P. Hoeflich,[1] C. R. Burns,[5] C. Gall,[4,6] E. Y. Hsiao,[1] M. M. Phillips,[7] N. Morrell[7] and Ryan J. Foley[8]

[1]*Department of Physics, Florida State University, Tallahassee, FL 32306, USA*
[2]*Astrophysics Research Institute, Liverpool John Moores University, IC2, Liverpool Science Park, 146 Brownlow Hill, Liverpool L3 5RF, UK*
[3]*Max-Planck-Institut für Astrophysik, Karl-Schwarzschild-Str. 1, D-85748 Garching, Germany*
[4]*Department of Physics and Astronomy, Aarhus University, Ny Munkegade 120, DK-8000 Aarhus C, Denmark*
[5]*Observatories of the Carnegie Institution for Science, 813 Santa Barbara St, Pasadena, CA 91101, USA*
[6]*Dark Cosmology Centre, Niels Bohr Institute, University of Copenhagen, Juliane Maries Vej 30, DK-2100 Copenhagen Ø, Denmark*
[7]*Carnegie Observatories, Las Campanas Observatory, 601 Casilla, La Serena, Chile*
[8]*Department of Astronomy and Astrophysics, University of California, Santa Cruz, CA 95064, USA*

Accepted 2018 February 23. Received 2018 February 23; in original form 2017 December 19

ABSTRACT

Radiative transfer models of two transitional type Ia supernovae (SNe Ia) have been produced using the abundance stratification technique. These two objects – designated SN 2007on and SN 2011iv – both exploded in the same galaxy, NGC 1404, which allows for a direct comparison. SN 2007on synthesized 0.25 $M_\odot$ of ^{56}Ni and was less luminous than SN 2011iv, which produced 0.31 $M_\odot$ of ^{56}Ni. SN 2007on had a lower central density (ρ_c) and higher explosion energy (E_{kin} ~1.3 ± 0.3 × 10^{51}erg) than SN 2011iv, and it produced less nuclear statistical equilibrium (NSE) elements (0.06 $M_\odot$). Whereas, SN 2011iv had a larger ρ_c, which increased the electron capture rate in the lowest velocity regions, and produced 0.35 $M_\odot$ of stable NSE elements. SN 2011iv had an explosion energy of ~E_{kin} ~0.9 ± 0.2 × 10^{51}erg. Both objects had an ejecta mass consistent with the Chandrasekhar mass (Ch-mass), and their observational properties are well described by predictions from delayed-detonation explosion models. Within this framework, comparison to the sub-luminous SN 1986G indicates SN 2011iv and SN 1986G have different transition densities (ρ_{tr}) but similar ρ_c. Whereas SN 1986G and SN 2007on had a similar ρ_{tr} but different ρ_c. Finally, we examine the colour–stretch parameter s_{BV} versus L_{max} relation and determine that the bulk of SNe Ia (including the sub-luminous ones) are consistent with Ch-mass delayed-detonation explosions, where the main parameter driving the diversity is ρ_{tr}. We also find ρ_c to be driving the second-order scatter observed at the faint end of the luminosity–width relationship.

Key words: radiative transfer – techniques: spectroscopic – stars: abundances – supernova: general – supernovae: individual (SN 2007on, 2011iv).

1 INTRODUCTION

Type Ia supernovae (SNe Ia) are thought to originate from the thermonuclear disruption of a Carbon–Oxygen (C–O) white dwarf(s) (WD) in a binary system. The two favoured progenitor channels are the single-degenerate scenario (SDS) and the double-degenerate scenario (DDS). In the SDS, a C–O WD accretes material from a non-electron degenerate companion star, either a main sequence, Helium or Red Giant star (Whelan & Iben 1973; Livne 1990; Nomoto & Kondo 1991; Woosley & Weaver 1994; Livne & Arnett 1995; Nomoto, Iwamoto & Kishimoto 1997). In the DDS, the binary system consists of two C–O WDs (Iben & Tutukov 1984; Webbink 1984). Recently, another scenario has been proposed where the orbit of two WDs are perturbed by a tertiary or quaternary companion, resulting in the direct collision of the WDs (Raskin et al. 2009; Rosswog et al. 2009; Kushnir et al. 2013; Dong et al. 2015; Fang, Thompson & Hirata 2017).

There are several potential explosion mechanisms for SNe Ia. In the merger of two WDs, the decreasing orbital radius reaches

★E-mail: chris.ashall24@gmail.com

the point where the binary system becomes unstable and the two WDs spiral in on a dynamical time-scale (Dan et al. 2014, 2015), and subsequently, the explosion is triggered by heat released during the merging process. Whereas in the collision scenario, the binary system loses angular momentum due to the presence of a third star, until the binary orbit becomes so eccentric that a collision can occur, with some non-zero impact parameter. In this case, the relative speed is close to the escape velocity and a detonation is unavoidable (Kushnir et al. 2013).

When a WD approaches the Chandrasekhar mass (Ch-mass), the explosion can be triggered by compressional heat near the WD centre (Diamond, Hoeflich & Gerardy 2015). This is usually thought to be in the SDS, although the accreted material in this scenario may also originate from a tidally disrupted WD in a double-degenerate system with accretion on a secular time-scale (Piersanti et al. 2003). Finally, explosions of a sub-Ch-mass WD in the SDS can be triggered by detonating the surface He layer, which drives a shock wave igniting the centre, producing a so-called double detonation explosion (Nomoto 1980; Nomoto, Thielemann & Yokoi 1984; Woosley & Weaver 1994; Höflich & Khokhlov 1996; Livne & Arnett 1995; Jiang et al. 2017). Current evidence seems to suggest that explosions near the Ch-mass seem to favour observations (see e.g. Mazzali et al. 2007; Hoeflich et al. 2017).

In Ch-mass explosions, the nuclear flame front proceeds as either a deflagration (less than the local sound speed) or a detonation (faster than the local sound speed), but recent work has shown it is not possible to reach a progenitor configuration that can achieve a pure detonation by an accreting WD (Höflich & Stein 2002; Zingale et al. 2005). Also, pure deflagration models do not produce enough ^{56}Ni to power the brightest SNe Ia (Reinecke, Hillebrandt & Niemeyer 2002); moreover, these models fully mix the elemental abundances in the ejecta, which is in direct disagreement with observations of a chemically layered structure (Gamezo et al. 2003; Stehle et al. 2005; Jordan et al. 2012). Therefore, one of the most popular models is the delayed detonation (a deflagration with a transition to a detonation) explosion. In a delayed detonation explosion, an initial deflagration phase lifts the WD in its potential and partially unbinds the star, after which the flame front drops to a transition density ($\rho_{\rm tr}$) and a detonation is triggered. For a normally bright SNe Ia, to first order, $\rho_{\rm tr}$ determines the amount of ^{56}Ni synthesized in the ejecta, as there is more effective burning during the detonation phase (Khokhlov 1991; Höflich et al. 2002; Gamezo et al. 2003).

A variation on the delayed detonation scenario is the pulsation-delayed detonation (PDD) explosion. This is where the WD stays bound after the deflagration phase, and undergoes a pulsation prior to the deflagration to detonation transition. The amount of burning in the deflagration phase determines if the WD is strongly or weakly bound; more burning reduces the binding energy of the WD. PDDs can be produced with varying mass and amplitude pulsations, and can explain some of the diversity amongst SNe Ia (Höflich et al. 1996; Dessart et al. 2014; Stritzinger et al. 2015).

Hydrodynamical models of deflagration fronts indicate that they are multidimensional in nature, and strongly mixed by Rayleigh–Taylor instabilities (Zel'dovich 1970; Khokhlov 1995; Gamezo et al. 2003; Livne, Asida & Höflich 2005; Röpke et al. 2007; Seitenzahl et al. 2013). However, from observations there is strong evidence that there is an additional process that is needed to suppresses the mixing. Observations include (i) direct imaging of the supernova remnant s-Andromeda that shows a large Ca-free core indicative of high-density burning and limited mixing (Fesen et al. 2007; Fesen & Milisavljevic 2016; Fesen et al. 2017), (ii) significantly degraded spectral fits by models that have an injection of radioactive material into the Si/S layers (Höflich et al. 2002), and finally, (iii) the presence of pot-bellied line profiles observed in spectra obtained 1–2 yr after the explosion thought to be formed from a significant amount of stable Fe-group isotopes located in the central region of the ejecta (Höflich et al. 2004; Motohara et al. 2006; Maeda et al. 2010a,b; Diamond et al. 2015; Stritzinger et al. 2015).

The cause of this suppression is currently unknown, but magnetic fields may have something to do with it (Höflich et al. 2004; Penney & Hoeflich 2014; Remming & Khokhlov 2014), and show promising results (Hristov et al. 2017), as well as rapid rotation in the initial WD (Uenishi, Nomoto & Hachisu 2003; Yoon & Langer 2005).

Furthermore, observational evidence strongly suggests that SNe Ia are spherical. This includes the overall spherical density distributions as shown by low-continuum polarization (Maund et al. 2010; Patat et al. 2012) and spherical SNe Ia remnants exhibiting evidence of a chemical layered structure (Rest et al. 2005; Fesen et al. 2007). Spherical delayed detonation models such as those from Hoeflich et al. (2017) naturally suppress the mixing and does account for all of these observational traits.

The first-order SNe Ia can be characterized by their luminosity-decline rate ($\Delta m_{15}(B)$, stretch) relation (Phillips et al. 1999), and the luminosity–colour relation (Tripp 1998). The amount of ^{56}Ni in the ejecta determines the peak luminosity of the light curve (Arnett 1982), and the link between ^{56}Ni, luminosity, and opacity determines the light-curve shape (Mazzali et al. 2001). Using these empirically derived relations to calibrate the observed luminosity of SNe Ia allows them to serve as powerful extragalactic distance indicators used to study the expansion history of the Universe. For example, the comparison of a low-redshift and high-redshift SNe Ia samples provided the first direct evidence of accelerated expansion of the Universe (e.g. Perlmutter et al. 1999; Riess et al. 1998, 2016).

There are many sub-types of SNe Ia, including fast declining and sub-luminous (1991bg-like SNe Ia), ($\Delta m_{15}(B)$>1.8 mag), as well as transitional SNe Ia. Transitional SNe Ia sit in an area of parameter space between normal and 1991bg-like SNe Ia, have a $\Delta m_{15}(B)$ between 1.6 and 2.0 mag, and are rare objects (Ashall et al. 2016). Some examples of transitional SNe Ia are SN 1986G (Phillips et al. 1987; Ashall et al. 2016), 2003hv (Leloudas et al. 2009), iPTF 13ebh (Hsiao et al. 2015), and SN 2015bp (Srivastav et al. 2017).

Theoretically, it has been proposed that 1991bg-like SNe Ia could come from a different type of progenitor system than that of normal SNe Ia. Some of the suggested scenarios are sub-Ch-mass explosions (Stritzinger et al. 2006; Blondin et al. 2017), mergers of two WDs (Pakmor et al. 2010; Mazzali & Hachinger 2012), or delayed detonation explosion of Ch-mass WDs (Höflich et al. 2002). Furthermore, it has recently been suggested by Blondin et al. (2017) that SNe Ia with $\Delta m_{15}(B)$>1.4 mag and by Goldstein & Kasen (2018) that SNe Ia with $\Delta m_{15}(B)$>1.55 mag, can only be produced by sub-Ch-mass explosions. Therefore, understanding transitional SNe Ia and their link between normal and 1991bg-like objects is critical, as it will help us to determine whether or not sub-luminous SNe Ia come from a distinct population.

Transitional SNe Ia are rare and have not yet been studied in detail, but one transitional SN Ia (SN 1986G) has been shown to be consistent, a delayed detonation Ch-mass explosion with a high central density (ρ_c) (Ashall et al. 2016). However, this is only one example, and the sub-class of transitional SNe Ia have a diverse set of properties. Three important questions that need to be answered are: (1) Do any transitional SNe Ia begin to diverge from the Ch-mass? (2) What causes the diversity in fast-declining SNe Ia? and

(3) Do transitional SNe Ia provide a smooth link between the normal and sub-luminous SNe Ia populations?

Today errors in the estimated cosmological parameters are limited not by sample sizes, but by a number of systematics, such as errors in photometric calibration and understanding the SNe Ia intrinsic colour and dust relations. Whilst there are many efforts to address these problems such as Rheault et al. (2010), Stubbs et al. (2010), and Sasdelli et al. (2016), another more promising route is to fully understand the physics of the explosions. This was one of the main objectives of the *Carnegie Supernova Project* (CSP), and has produced some promising results (see e.g. Folatelli et al. 2012; Burns et al. 2014; Gall et al. 2018). To further improve our understanding of the Universe, and to be able to determine which of the competing cosmological models correctly describes its expansion history, we need to obtain errors on the distances to SNe Ia at the ∼1 per cent level. To do this, understanding what causes the intrinsic variations between SNe Ia is key. With this in mind, we set out to understand the explosion physics of two transitional SNe Ia (2007on and 2011iv), as well as the overall properties of the transitional SNe Ia population.

Comprehensive data sets of SNe 2007on and 2011iv have recently been presented by Gall et al. (2018). Both of these objects were located in NGC 1404, with SN 2007on exhibiting a decline rate of $\Delta m_{15}(B) = 1.96 \pm 0.01$ mag and SN 2011iv exhibiting decline rate of $\Delta m_{15}(B) = 1.77 \pm 0.01$ mag. Both objects have features consistent with normal SNe Ia including (i) no Ti II feature at ∼4500 Å at maximum (ii) they both peak in the near-infrared bands prior to the optical bands, and (iii) they both exhibit a secondary maximum in the near-infrared bands. They also show features indicative of sub-luminous SNe Ia including (i) a high Si II line (∼5970–6355 Å) ratio[1] (ii) and a fast-evolving light curve. These characteristics suggest that their photospheres are in the temperature regime located just above those of sub-luminous SNe Ia.

The ^{56}Ni mass inferred from the peak luminosity, using Arnett's rule, estimated from the UVOIR light curves presented by Gall et al. (2018), correspond to $0.25 \pm 0.05\,M_\odot$ for SN 2007on and $0.42 \pm 0.06\,M_\odot$ for SN 2011iv. This compares to $0.32\,M_\odot$ for SN 2007on and $0.37\,M_\odot$ for SN 2011iv from Hoeflich et al. (2017), and to $0.17^2\,M_\odot$ for SN 2007on and $0.41^3/0.32^4\,M_\odot$ for SN 2011iv as estimated from the nebular phase models of Mazzali et al. (2018).

One intriguing characteristic found when comparing the $B - V$ colour evolution of SN 2007on and SN 2011iv is the fact that at early times the latter is brighter and bluer than the former, but after +20 d relative to B-band maximum and extending past +85 d, SN 2007on is 0.12 mag bluer than SN 2011iv. Gall et al. (2018) speculate this is due to differences in ρ_c with their delayed detonation models predicting bluer colours at late time as a function of decreasing ρ_c. This 0.12 mag difference in $B - V$ colours therefore suggests that SN 2007on had a ρ_c about half of that of SN 2011iv. Another intriguing feature about SN 2007on is its multiple emission peaks in the nebular phase (Dong et al. 2015). In a companion paper, Mazzali et al. (2018) demonstrate that these peaks are possibly due to two different components, one redshifted and one blueshifted, with similar ejecta and ^{56}Ni masses but different degrees of ionization. These components suggest that SN 2007on is either a very off-centre delayed detonation explosion of a (near) Ch-mass WD, or a collision of two similar mass WDs. In either case, both scenarios agree that SN 2007on had a lower ρ_c than SN 2011iv.

In this paper, we perform a detailed radiative transfer synthetic spectral analysis on both SN 2007on and SN 2011iv, in order to explain their differences and propose a progenitor scenario for their explosions. The method we use is the abundance stratification technique. Abundance stratification utilises the fact that as time passes deeper and deeper layers of the expanding ejecta are revealed. Therefore, a time series of spectra can be used to determine key properties of the SN Ia, including the abundance distribution (in velocity and mass space) of various elements in the ejecta, which reveal themselves through spectral line features. This technique has been used for many SNe Ia, including SNe Ia 2002bo (Stehle et al. 2005), 2003du (Tanaka et al. 2011), 2004eo (Mazzali et al. 2008), the very nearby SNe 2011fe (Mazzali et al. 2014) and 2014J (Ashall et al. 2014), and the transitional SN 1986G (Ashall et al. 2016), as well as core-collapse SNe (e.g. Ashall et al. 2017; Prentice et al. 2017; Mazzali et al. 2018). It was also applied to SN 2011ay (Barna et al. 2017) using a different modelling code. In this paper, we demonstrate how both SNe 2007on and 2011iv fit into the transitional and sub-luminous SNe Ia paradigm. Finally, we review the area of transitional and fast-declining SNe Ia, as well as the s_{BV} versus $L_{\max}$ relation.

2 MODELLING TECHNIQUE

The abundance stratification technique makes use of the fact that an SN explosion can be split into two physically distinct parts: the photospheric and nebular phases. The results from the photospheric phase modelling can be used as an input for the nebular phase modelling. This allows us to probe the full abundance distribution in velocity and mass space.

A SN ejecta can be thought to be in homologous expansion ∼10 s after explosion. This is estimated by the equation $r = v_{\rm ph} \times t_{\rm exp}$, where r is the distance from the centre of the explosion, $v_{\rm ph}$ is the photospheric velocity, and $t_{\rm exp}$ is the time from explosion. Hence, as time passes deeper and deeper layers of the explosion can be seen.

At early times the ejecta are dense enough to emit continua within itself, producing an effective photosphere. This photosphere is actually a line-dominated pseudo-photosphere, as line blanketing is the dominant source of opacity in an SN ejecta (Pauldrach et al. 1996). Therefore, the Schuster–Schwarzchild approximation is used in our code. This approximation assumes that radiative energy is emitted from an inner blackbody. The radiation transport is then calculated above this pseudo-photosphere. The Schuster–Schwarzchild approximation is very useful as it does not require an in-depth knowledge of the radiation transport below the photosphere, but it still yields good results. However, at later times after bolometric maximum, this approximation can cause excess flux in the red (>6500 Å), but as most of the SN Ia lines are in the blue, this excess flux will not affect the results with respect to abundances derived.

The code is a 1D Monte carlo (MC) radiative transport code (Mazzali & Lucy 1993; Lucy 1999; Mazzali 2000). It simulates the emission of photon packets at a photosphere, and traces their evolution through an SN atmosphere. These packets can undergo Thomson scattering and line absorption. If the latter occurs, the packet is immediately re-emitted, following a branching scheme.

[1] The Si II line ratio is an indirect measurement of temperature as the Si II 6355 Å features becomes saturated, and as Si III recombines, it populated more excited levels (the 5970 Å feature) of Si II. This has the effect of increasing the line ratios (Nugent et al. 1995; Hachinger et al. 2008).
[2] Calculated below 4000 km s^{-1} using a two-component model.
[3] Calculated using a one-zone model.
[4] Calculated using a two-component model.

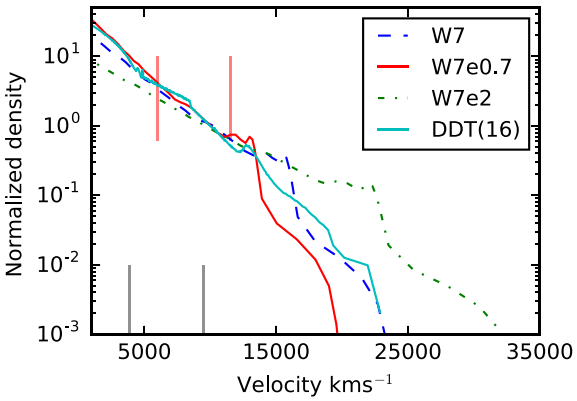

Figure 1. The W7 (dashed blue), W7e0.7 (solid red), W7e2 (dashed-dotted green), and DDT(16) density profile from Hoeflich et al. (2017), normalized to 10 000km s^{-1}. The vertical lines show the v_{ph} range for SN 2007on (back) and SN 2011iv (red).

This branching scheme allows fluorescence (blue to red) and reverse fluorescence (red to blue) to take place. Both of these are critical in forming an SN Ia spectrum. Fluorescence makes the optical part of the spectrum and reverse fluorescence to the UV. Packets that scatter back into the photosphere are reabsorbed; therefore, the blackbody temperature (T_{BB}) is iterated to match the input bolometric luminosity (L_{bol}), given the back scattering rate.

Ionization and excitation are treated using a modified nebular approximation to account for non-local thermodynamic equilibrium (NLTE) effects caused by the radiation field (Mazzali & Lucy 1993; Mazzali 2000). The radiation field and the state of the gas are iterated until convergence is reached. The final spectrum is computed using the formal integral to reduce Poisson noise (Lucy 1999).

The aim of the abundance stratification technique is, starting with the earliest spectrum, to vary input parameters such as abundance, v_{ph}, and L_{bol} to produce optimally fitting synthetic spectra. Before the free parameters can be varied, the density profile, distance, and extinction to the SNe must be set. Previous work on spectral modelling of normal SNe Ia tended to use the W7 density profile (Stehle et al. 2005; Ashall et al. 2014). The W7 model is a fast deflagration that synthesized 0.5–0.6 M$_\odot$ ^{56}Ni in the inner layers of the star, and has a kinetic energy (E_{kin}) of 1.3×10^{51} erg. However, in this work we start with the same density profile required for SN 1986G due to its similarities to SN 2007on and SN 2011iv. SN 1986G has been shown to be consistent with a low-energy W7-like density (Ashall et al. 2016). For convenience, we will call this model W7e0.7 as it has a E_{kin} 70 per cent of the standard W7 model, i.e. $E_{kin} = 0.9 \times 10^{51}$ erg. When the W7e0.7 produces inadequate results (i.e. a poor fit to the observed spectra), we also test the W7 and W7e2 ($E_{kin} = 2.6 \times 10^{51}$ erg) density profiles. This is done to demonstrate how different values of E_{kin} will affect the models.[5]

We note that the density profile of the deflagration model W7 is very similar to the structure of a delayed detonation model for transitional SNe Ia. In both cases, material with more than 14 000 km s^{-1} is largely unburnt and as a consequence the density structure shows a 'bump' at the same velocity, and higher densities compared to normal-bright delayed detonation models. Fig. 1 shows the density profiles of the W7, W7e0.7, W7e2 models as well as DDT(16) from Hoeflich et al. (2017). It should be noted how similar the W7e0.7 and DDT(16) density profiles are, especially in the spectral formation region. Therefore, the assumption of using a W7-like profile holds. However, the similarity between W7-like profiles and delayed detonation models is only true for 'transitional' SNe Ia.

Transitional and sub-luminous SNe Ia are highly sensitive to physical second-order parameters such as ρ_c (Hoeflich et al. 2017); therefore, it is uncertain how accurately these objects can be used as distance indicators. It is known that sub-luminous and transitional SNe Ia tend to favour early-type galaxies (Hamuy et al. 1996; Ashall et al. 2016), with SNe 2007on and 2011iv being no exception. Both were located in the same early-type galaxy (NGC 1404) and suffer from almost no detectable host galaxy extinction.[6] This makes them an excellent case to test the accuracy of current methods for calculating distances to transitional SNe Ia. Gall et al. (2018) found that even after correcting for stretch and colour (extinction) both objects exhibit significantly different peak magnitudes, and the relative distances derived to them vary significantly. The distances they derived to the SNe differ by 14 per cent if the B-band was used, and 9 per cent if the H band was used. If SNe Ia are to be utilized as more precise cosmological rulers, understanding the diversity in their physics, and linking this back to light-curve fitting tools, is essential. Utilizing explosion models and physical second-order effects, Hoeflich et al. (2017) determined the distance modulus to the SNe to be consistent with each other and in the range of 31.2–31.4 mag.

Here, we use the independent method of spectral modelling to refine the distance to the SNe. By producing one-zone models, the distance to the SNe can be varied within a range until an optimal fit for both objects is determined. For SN 2007on and SN 2011iv, a distance modulus of 31.2 ± 0.2 mag was found to produce the best fit, i.e. the correct line ratios, ionization, and velocity (see Appendix A). This is fully consistent with the value calculated in Hoeflich et al. (2017). Furthermore, for SN 2011iv (the object with the more complete data set), Hoeflich et al. (2017) determine the same distance modulus derived in this work (i.e. 31.2 mag).

Once the extinction, distance, and density profile are set, the main part of the modelling procedure can take place. Starting with the earliest spectra, L_{bol} and v_{ph} are first determined and a typical abundance distribution is assumed. There are usually 2 or 3 synthetic shells placed above the photosphere in order to produce a stratified abundance distribution at high velocities. The abundances of the photospheric shell are varied until an optimal solution is found. The next spectrum is then modelled, and only the abundances inside the previous photosphere are changed. Abundances in the outer layers can affect the synthetic spectra at later epochs, as elements well above the photosphere can produce opacity (usually at a higher velocity relative to the observations) if there is large enough masses and densities in the outer shells of models. If this is the case iteration is required on the abundances of the elements in the outer layers. Abundances given in this work have an error of ± 25 per cent, and photospheric velocities have an error of ± 15 per cent. A full detailed analysis of the errors from the abundance stratification method can be found in (Mazzali et al. 2008). We note that with this method the existence of one good fit does not exclude other scenarios.

[5] We choose to stick to three models with a range of properties, as it gives us a range of results to choose from. It also avoids the subjective nature of determining the best fits, which can occur when a fine grid is used.

[6] All of the spectra in this work were corrected for $E(B-V)_{MW} = 0.01$ mag (Gall et al. 2018).

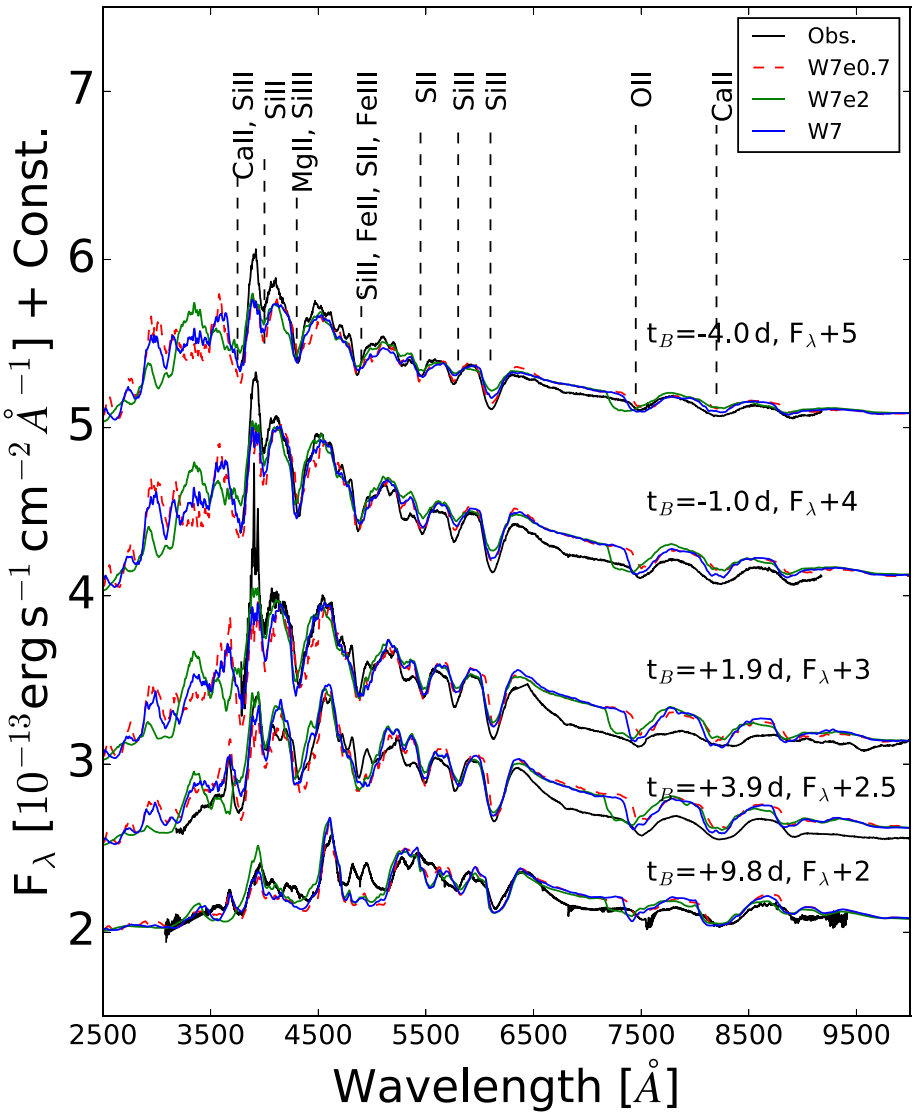

Figure 2. Time-series of photospheric phase visual-wavelength spectroscopy of SN 2007on (black lines) compared with models produced using three density profiles W7 (blue solid line), W7e0.7 (red dashed line), and W7e2 model (green solid line). The time relative to *B*-band maximum and the constant flux offset is plotted next to each spectrum.

3 PHOTOSPHERIC PHASE

In this section, we present the photospheric phase models of SNe 2007on and 2011iv. All of the data used in this paper were first published in Gall et al. (2018). A summary of the spectra, and its phase relative to *B*-band maximum, can be found in Tables B1 and B2.

3.1 SN 2007on

Five photospheric phase spectra of SN 2007on, from 12.8 to 26.6 d after explosion, were modelled (see Fig. 2).

The spectra are dominated by the standard SN Ia features, including (Ca II λλ3933, 3968; Si II λλ4128, 4130; Mg II λ4481; Si III λλ4552, 5978, 6347, 6371; Fe II λλ4923, 5169; Fe III λ5156; S II λλ5432, 5453, 5606; O I λλ7777, 7774, 7774; and Ca II λλ8498, 8542, 8662). The input parameters of the models can be found in Table 1. The photospheric velocity of SN 2007on covers a range from 3900 to 9500 km s^{-1}, and a rise time of 16.8 ± 0.5 d has been used, implying that SN 2007on exploded on JD 2,454,403.5.

Table 1. Input parameters for the photospheric models of SN 2007on.

Epoch $t_{\rm rise}$ [a]	Phase $t_{\rm peak}$ [b]	Velocity $v_{\rm ph}$	UVOIR $L_{\rm max}$ $\log_{10}(L_{\rm max})$
days	days	km s^{-1}	erg s^{-1}
12.8	−4.0	9500	42.37
15.8	−1.0	9200	42.50
18.7	+1.9	8700	42.50
20.7	+3.9	6600	42.44
26.6	+9.8	3900	42.19

[a] Days since inferred explosion time (JD 2454 403.5).
[b] Rest-frame time relative to *B*-band maximum (JD 2454 420.4).

Due to the lack of early and UV data of SN 2007on, we cannot test the metallicity of the progenitor, or the composition of the outermost layers of the ejecta, but we can determine the basic properties and

abundances of the explosion. We note that although the inner layers of SN 2007on are made of two components (see Mazzali et al. 2018), at early times these components will be hidden below the optically thick photosphere; hence, our modelling results are still valid.

The fits from the model made with the W7e0.7 density profiles (see Fig. 2) are reasonable, but do show signs of being too hot: the spectrum has a large Si III absorption at ∼4400 Å. Therefore, we made models with the W7 and W7e2 density profiles. The W7e2 model has too much oxygen absorption at high velocities, as seen in the ∼7500 Å feature. This is caused by an enhanced density in the outermost layers where oxygen is dominant. The W7 model produces the best fits, and is therefore our preferred choice. Below we discuss the results from the W7 model at three distinct epochs.

3.1.1 −4.0 d

The earliest spectrum of SN 2007on was obtained 12.8 d after explosion. The $v_{\rm ph}$ at this epoch is 9500 km s^{-1}; at this velocity, there is ∼0.6 $M_{\rm ej}$ of material above the photosphere. Going from blue to red, the main lines that contribute to the spectrum are Ca II λλ3934, 3968; Si II λλ4131, 4128; Mg II λλ4481.13, 4481.32; Si III λλ4553, 4568, 4575; Si II λλ5041, 5056; Fe II λλ5018, 5169; S II λλ5009, 5032, 5212, 5432, 5453, 5606; Si II λλ5957, 5978, 6347, 6371; O I λλ7772, 7774, 7775; Ca II λλ8542, 8662; and Mg II λλ9218, 9244. Even at this early epoch, there is very little Fe III absorption in the model, as is seen in the narrowness of the 4800 Å feature (see Fig. 2).

3.1.2 +1.9 d

The model at 18.7 d after explosion has a v_{ph} of 8700 km s^{-1}. The spectrum is similar to the one obtained at −4.0 d, except for a few notable differences, which are (i) the feature at 4400 Å contains no contribution from Si III λλ4553, 4568, 4575; (ii) Co II λλ4136, 4660 lines are seen in the 4400 Å feature, this Co II is produced from the decay of ^{56}Ni located above the photosphere, (iii) there are blends of Co II e.g. λλ3446, 3501, 3621 lines in the near UV.

3.1.3 +9.8 d

The model at 26.6 d after explosion shows a lot of evolution with respect to the previous epoch, especially in the blue part of the spectrum. Due to the adiabatic expansion of the ejecta, the spectrum is significantly redder and cooler than previous epochs. Most of the Ti abundance at this phase is singly ionized (i.e. Ti II λλ3446, 3501, 3621), whereas in the model at +1.9 d almost all of the Ti was doubly ionized (i.e. Ti III). The 3000−4000 Å region contains blends of Ti II and Co II (e.g. λλ3446, 3501, 3621) lines as well as Ca II λλ3934, 3968. The strongest lines in the feature at ∼4300 Å are Si II λλ4131, 4128 and Ti II λλ4395, 4444, 4469; however, this feature also contains blends of lines from many ions including Co II, Ni II, Mg II, Cr II, and Fe II. The feature at 4900 Å contains significant contribution from Fe II λλ4924, 5018, 5169; Si II λλ5041, 5056; and Fe III λλ5156, 5127, 5074.

3.2 SN 2011iv

Fig. 3 contains the comparison between the observations (black) and the photospheric phase models (blue) of SN 2011iv, produced with the W7e0.7 density profile. As these models produce good fits to the data, and Ashall et al. (2016) test multiple density profiles for transitional SNe Ia, we do not test other density profiles for SN 2011iv. The spectra are dominated by normal SNe Ia features (Ca II λλ3933, 3968; Si II λλ4128, 4130; Mg II λ4481; Si III λλ4552, 5978, 6347, 6371; Fe II λλ4923, 5169; Fe III λ5156; S II λλ5432, 5453, 5606; O I λλ7777, 7774, 7774; and Ca II λλ8498, 8542, 8662), and were observed from −6.6 d to +13.3 d relative to *B*-band maximum light.

Generally, the models fit the observed spectra well, including in the UV. The input for the models of SN 2011iv can be seen in Table 2. The photospheric velocity covers a range of 5500 km s^{-1}, with the largest photospheric velocity being 11 500 km s^{-1}. In our models, the bolometric luminosity peaks at 18.4 d after explosion. At this point, the photosphere is approximately half way through the ejecta, and has a velocity of 9500 km s^{-1}.

An SN Ia spectrum develops over the course of months, and except at very early times, there is only a small evolution over the course of a single day. Therefore, we discuss the models and spectra of SN 2011iv at four epochs, −5.5 d, +0.4 d, +4.4 d, +13.3 d.

3.2.1 −5.5 d

The earliest spectrum, with UV data, of SN 2011iv was observed at −5.5 d relative to *B*-band maximum. The $v_{\rm ph}$ at this epoch is 10 200 km s^{-1}. The main lines that contribute to each feature are identified in the top left-hand panel of Fig. 4. In an SN, photons emitted at the photosphere can only escape the ejecta when they reach an 'available' frequency at which they will not interact with any spectral lines. However, due to the relative expansion of the ejecta, and therefore Doppler overlapping of lines, the next available frequency for a photon to escape can be significantly redward relative to the frequency at which it was emitted from the photosphere. In the UV part of the spectrum, this is a source of continuum opacity. This effect is known as line blanketing. Therefore, setting the flux level in the UV is important for forming the optical spectra.

The UV (<3500Å) of the −5.5 d spectrum consists of a blend of Co II, Fe II, Mg II, with some contributions from Ni II, Ti II, Ti III, and V II. The spectrum at wavelengths <2500 Å is dominated by Co II and Fe II lines, the strongest of these being Fe II λ2599 and Co II λ2580. In the wavelength region of 2500−3000 Å, there is a blend of metal lines including Fe II λ2755, Co II λ2663, and Ni II λ2510. The strongest lines in this region are the Mg II resonance duplet λλ2795, 2802. Moving reward, the features are all dominated by the typical SNe Ia spectral lines (see e.g. Ashall et al. 2014). The feature on the red side of the larger 4400 Å feature is caused by Si III λλ4552, 4567, 4574 lines, and it should be noted that the 4800 Å feature is dominated by Si II with only a small contribution from Fe III.

3.2.2 +0.4 d

The next spectrum with UV and optical data was the *HST* spectrum obtained close to *B*-band maximum. The model at this epoch produces a good fit to the data (see the top right-hand panel of Fig. 4). The $v_{\rm ph}$ is 9500 km s^{-1}, and the bolometric luminosity is $\log_{10}(L_{\rm bol})$ = 42.95 erg s^{-1}. Compared to the −5.5 d model, there has been some development of the spectrum, most noticeably the shape of the flux in the UV. In this spectrum and model, there is a clear double absorption feature at 3100 Å, and the shapes of the 4400 and 4800 Å features have also changed. The change in the 4400 Å feature is due to a lack of Si III in the maximum light model and

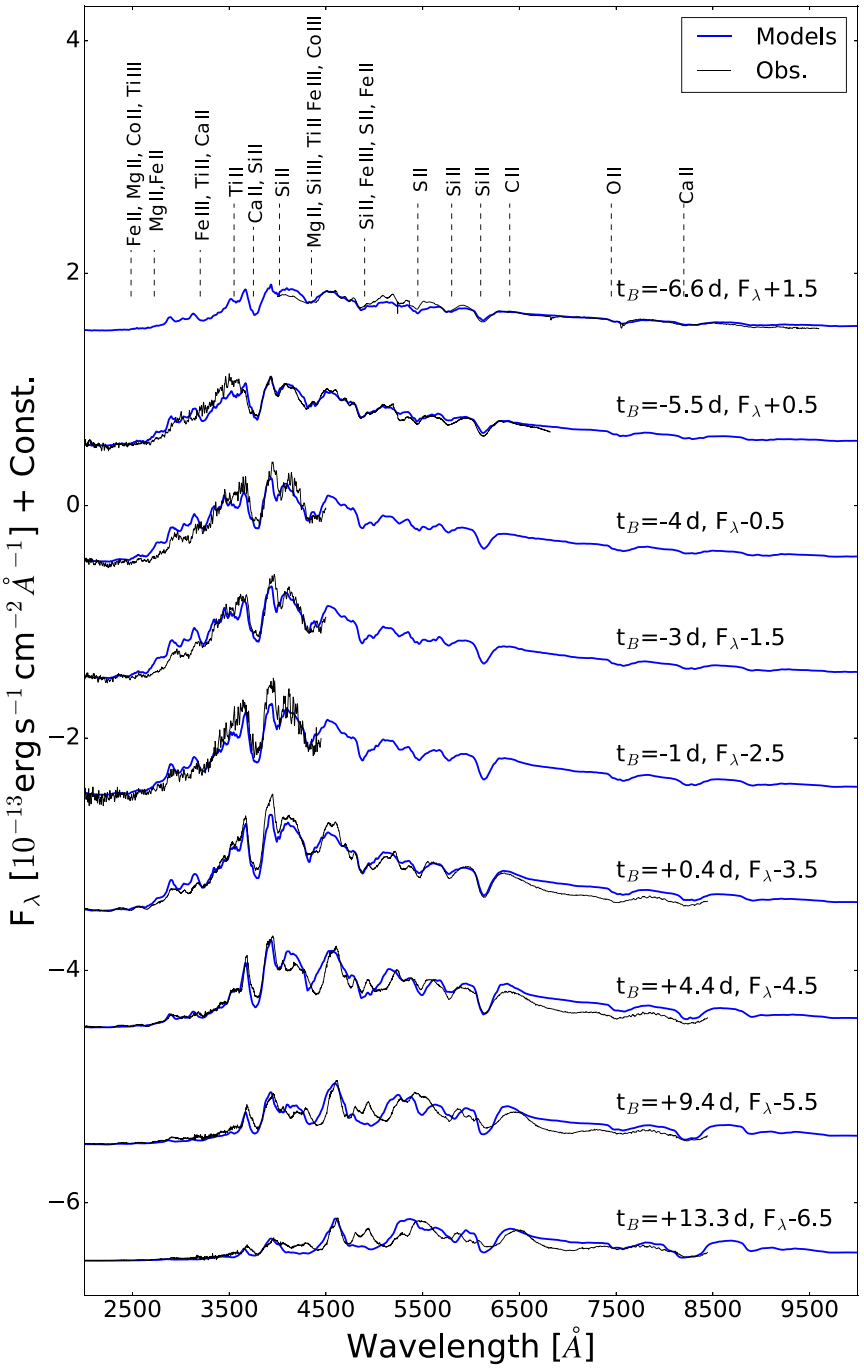

Figure 3. Time-series of photospheric phase visual-wavelength spectroscopy of SN 2011iv (black lines) compared to the synthetic models (blue lines). The models were computing using the W7e0.7 density profile. The time relative to *B*-band maximum and the constant flux offset is plotted next to each spectrum.

spectrum, and the difference in the red part of the 4800 Å feature is due to an increase in the strength of Fe III lines.

In the UV, the model fits the data exceptionally well. Once again the lines dominating this part of the spectrum and model are blends of metals, as well as the Mg II resonance line duplet. The double absorption feature at 3100 Å is dominated by weak V II lines λλ3093, 3102; Ti II λ3349; and Ti III λ2984. The reduced flux between 3300 and 3800 Å compared to previous epochs is caused by a blend of Co II lines.

3.2.3 +4.4 d

The +4.4 d *HST* spectrum and model are plotted in the bottom left-hand panel of Fig. 4. This model was 22.8 d after explosion. It is apparent at this epoch that the SN is much cooler. The model produces a satisfactory fit, and the quality of the model in the UV is very good. The excess flux in the red is due to the model using the Schuster–Schwarzchild approximation, but since most of the strong lines are at wavelengths less than 6500 Å, this does not affect the

Table 2. Input parameters for the photospheric models of SN 2011iv.

Epoch t_{rise}[a]	Phase t_{peak}[b]	velocity v_{ph}	UVOIR L_{max} $\log_{10}(L_{max})$
days	days	km s^{-1}	erg s^{-1}
11.8	−6.6	11500	42.64
12.9	−5.5	10200	42.81
14.4	−4.0	9700	42.87
15.4	−3.0	9600	42.91
17.4	−1.0	9550	42.93
18.8	+0.4	9500	42.95
22.8	+4.4	8200	42.90
27.8	+9.4	6600	42.77
31.5	+13.3	6000	42.65

[a]Days since inferred explosion time (JD 2455924.6).
[b]Rest frame-time relative to *B*-band maximum (JD 2455906.1).

results concerning line identification or abundances. In this model, the 4800 Å feature consists of Si II Fe II and Fe III.

3.2.4 +13.3 d

The photospheric velocity of the +13.3 d model is 6000 km s^{-1}. This is below ∼65 per cent of the 1.38 $M_\odot$ ejecta. The fits to the data are worse at this epoch, as this is where there is a significant fraction of ^{56}Ni, and therefore energy deposition, above the photosphere. However, the main absorption features are still seen in the models, and the flux in the UV is approximately correct (see the bottom right-hand panel of Fig. 4).

3.2.5 Metallicity and metal content of SN 2011iv

SNe Ia with different progenitor metallicities will produce varying amounts of ^{56}Ni and Fe-group elements. These elements can be

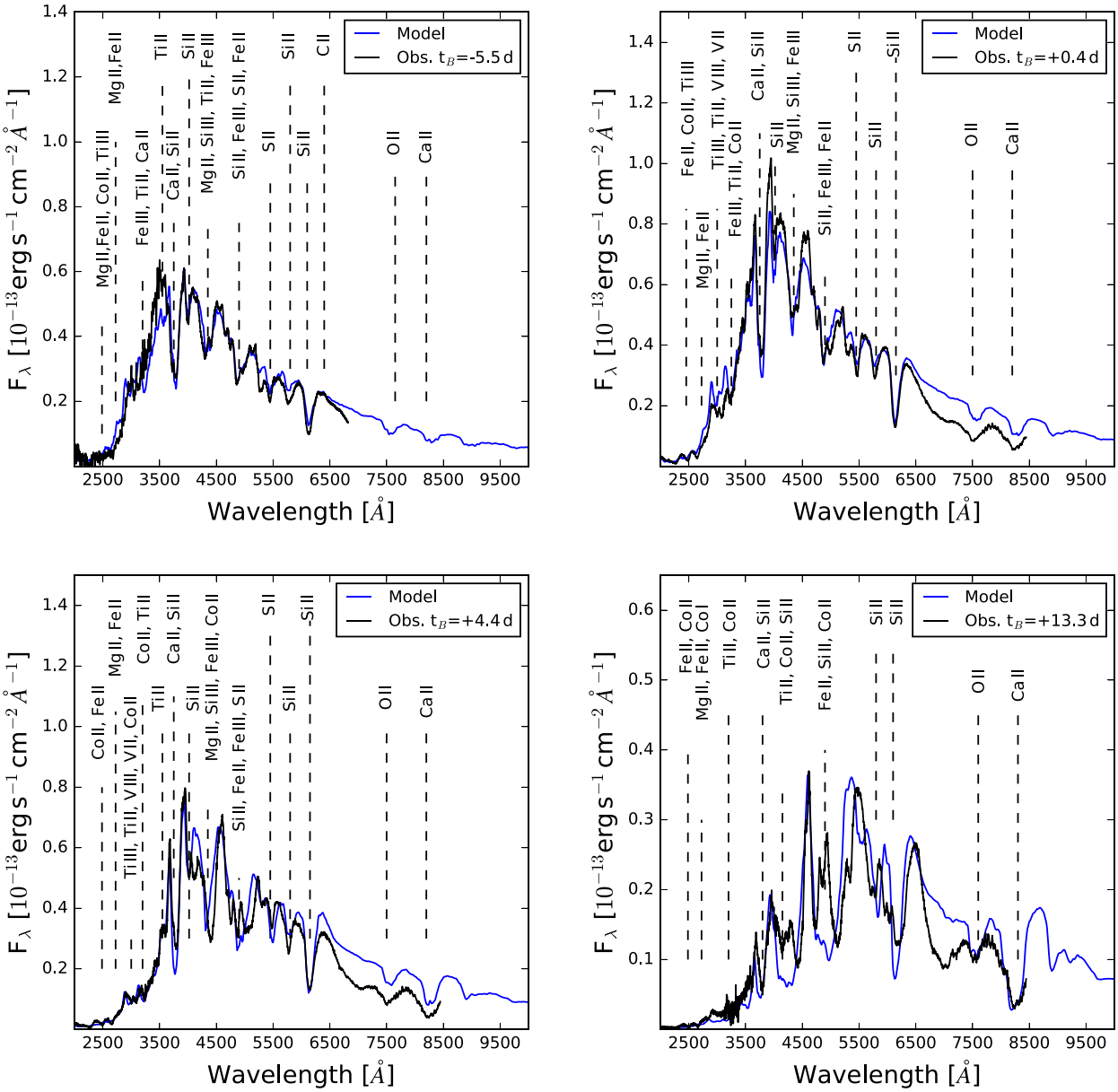

Figure 4. Spectrum (black) and model (blue) of SN 2011iv at −5.5 d (top left-hand panel), +0.4 d (top right-hand panel), +4.4 d (bottom left-hand panel), and +13.3 d (bottom right-hand panel) relative to *B*-band maximum.

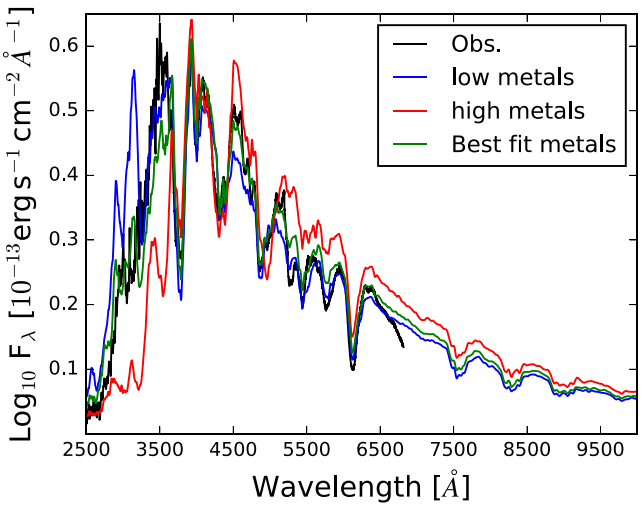

Figure 5. The observation (black) and three models with varying metal content of SN 2011iv at −5.5 d. The red model has an Fe abundance of 1.3 per cent above 15 000 km s^{-1}, the blue model has an Fe abundance of 0.03 per cent (i.e. a mass fraction $3\times\ 10^{-4}$) above 15 000 km s^{-1}, and the green model is the best fit with an Fe abundance of 0.3 per cent above 15 000 km s^{-1}.

distributed differently throughout the ejecta. The UV region of an SN Ia spectrum is where the abundance of ^{56}Ni and Fe-group elements can be best determined (e.g Lentz et al. 2000; Walker et al. 2012). It has been theorised that an increase in progenitor metallically may affect the amount of ^{56}Ni synthesized in SNe Ia, as a larger abundance of neutron-rich isotopes, such as ^{54}Fe and ^{58}Ni will be produced (Iwamoto et al. 1999; Timmes, Brown & Truran 2003; Bravo et al. 2010). This will affect the shape of an SN Ia light curve (Mazzali & Podsiadlowski 2006). The UV probes the area where metallically effects are also important, as a large number of metal line transitions are in this region. Photon packets that escape the SN ejecta in the UV must first be shifted to redder wavelengths further out in the ejecta before they can make a transition into the blue and escape the outer shell of the ejecta (Mazzali 2000).

The early-time UV flux of an SN Ia ejecta is very dependent on the metal content. The UV flux level plays a major part in forming the optical part of an SN spectrum. For example, a higher metal content increases the amount of absorption in the UV, and the amount of line blanketing. This increases the back scattering rate of photon packets into the photosphere, which increases the photospheric temperature. In the outermost layers, the flux in the UV is directly linked to the metallicity of the progenitor system, as nucleosythesis is expected to play a minor role. The spectrum obtained at −5.5 d relative to maximum is the earliest UV observation of SN 2011iv (see Fig. 5). The photospheric velocity at this shell is 10200 km s^{-1}, and there is ∼0.25 M$_\odot$ of ejecta above this photosphere. However, the amount of ejecta mass probed is a function of wavelength, and before maximum light the flux in the *u*-band probes the outermost 0.06 M$_\odot$ of ejecta, with the outermost ∼0.02 M$_\odot$ of ejecta being probed at −5.5 d[7] (Gall et al. 2018). Therefore, our models are probing the outermost layers of the SN explosion where the composition and metallically of the progenitor system can affect the observed spectra.

We have produced three one-zone models with varying metal abundances at −5.5 d (see Fig. 5). The best-fitting model has an Fe abundance of 0.3 per cent above 15 000 km s^{-1}, and an ^{56}Ni abundance of ∼1.5 per cent. The red model in Fig. 5 has an Fe abundance of 1.3 per cent above 15 000 km s^{-1} and the blue model has an Fe abundance of 0.03 per cent. The outer layers have metallicity larger than solar[8] (Asplund et al. 2009). If this high velocity, large metal abundance is not primordial, it is still likely to be linked to the metallicity of the progenitor WD. It has been demonstrated by many groups (see e.g. Höflich et al. 1998; Iwamoto et al. 1999) that a small increase in progenitor metallicity can dramatically increase the production of ^{54}Fe in the outer layers. This is because metallicity mainly affects the initial CNO abundances of a star, and therefore the proton-to-nucleon ratio (Y_e) decreases with increasing metallicity (Höflich et al. 1998). Conversely, in the low-velocity central regions of an SN Ia the temperatures are high enough that Y_e is determined by electron capture. Therefore, the large Fe abundance in the outer layers of SN 2011iv implies that the metallicity of the progenitor WD was super-solar. This is in agreement with what could be expected from an SN in a giant elliptical galaxy, such as NGC 1404.

3.3 Comparison between the photospheric results of SN 2007on and SN 2011iv

The early-time models of SN 2007on and SN 2011iv highlight the fact that around maximum they are similar objects, which can be identified by similar spectral lines. However, they do show some differences. For instance, the rise time and bolometric luminosity of SN 2011iv ($t_{\rm rise}$=18.4 d, $\log_{10}(L_{\rm max}) = 42.95$ erg s^{-1}) is larger than the equivalent values for SN 2007on ($t_{\rm rise}$ = 16.8 d, $\log_{10}(L_{\rm max})$ = 42.60 erg s^{-1}). Furthermore, the spectra of SN 2011iv tend to contain more doubly ionized species (e.g. Fe III) with respect to SN 2007on, although both have significantly less than a 'normal' SNe Ia. To first order the difference in rise time and light-curve shape of the objects is due to an opacity effect (as opacity is the main driver of light-curve shape) where the more luminous SN 2011iv produces more Fe through ^{56}Ni decay and therefore has a broader light curve (as line opacity dominates in SNe Ia, and Fe-group line contribute to the opacity by an order of magnitude more than those from intermediate-mass elements (IMEs; Mazzali et al. 2007). In Section 5, we examine the abundances obtained from the spectral modelling and further quantify the main reason for the difference between SN 2007on and SN 2011iv.

The other notable difference between the SNe is that the best models are produced with different density profiles. The preferred density for SN 2007on (W7) has more mass at higher velocities than the best density for SN 2011iv (W7e0.7). This implies that if SN 2007on is a Ch-mass explosion, it will have less mass in the inner layers relative to SN 2011iv, which agrees with the conclusions of Gall et al. (2018) who determine that SN 2007on had a lower ρ_c than SN 2011iv. Furthermore, Gall et al. (2018) found that around maximum light the Doppler velocity of the Si II λ6355 feature is larger in SN 2007on than SN 2011iv; this is in agreement with the results here that show that SN 2007on has a higher $E_{\rm kin}$ than SN 2011iv. Interestingly, the least luminous of the two SNe was produced from the more energetic explosion. This highlights the peculiarities of SN 2007on and hints that these objects may come from different progenitor scenarios or explosion mechanisms.

[7] We note that these values will be dependent on the explosion model used.

[8] These results could change depending on the underlying density profile used, and we note our results will be less sensitive at velocities over ∼19 000 km s^{-1}.

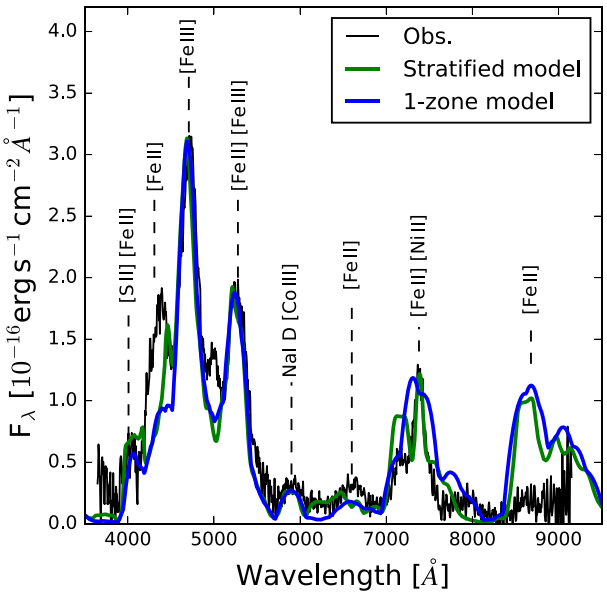

Figure 6. Nebular phase spectra (black), the one-zone model (blue), and the stratified model (green) of SN 2011iv at +276 d after explosion.

4 NEBULAR PHASE

The inner layers of SN 2007on may be formed of two separate components. SN 2007on is therefore the subject of a companion paper Mazzali et al. (2018). Hence, we do not discuss the nebular spectra of SN 2007on here.

4.1 SN 2011iv

The nebular spectrum of SN 2011iv was modelled using an NLTE code that was described in a series of papers (e.g. Mazzali et al. 2001). In order to test the general properties of the SN, we started with a one-zone model where the abundances are kept constant inside a sphere with limiting radius determined by the velocity of the emission lines. The epoch of the spectrum was 276 rest-frame days after explosion, or ∼260 d after *B*-band maximum (observed). The boundary velocity that led to best fits was selected as 9000 km s^{-1}. We built up the model trying to match the strongest features caused by the [Fe II] and [Fe III] emission lines (see e.g Mazzali et al. 2007). The spectrum is powered mainly by the decay of ^{56}Co, but the decay of ^{56}Ni also contributes. We found that in order to match the flux emitted in most of the strongest optical lines, an ^{56}Ni mass of 0.41 M$_\odot$ is required. The [Fe III]-dominated emission near 4700 Å is suppressed relative to the [Fe II]-dominated emission near 4300 Å. To produce the rather low observed ratio, ∼1.5, of the two strongest Fe lines, a significant amount of stable iron group elements (0.25 M$_\odot$ of stable iron and 0.09 M$_\odot$ of stable nickel) is necessary. These stable iron group elements contribute to cooling but not to heating, thereby reducing the ionization state. The stable nickel gives rise to an emission near 7300 Å, which matches the observed feature in flux but not in wavelength as the emission line is affected by significant blueshift. The model has a total mass ∼0.8 M$_\odot$ inside the boundary velocity (The nebular phase 1-zone model contains 0.05 M$_\odot$ of IMEs). This is consistent with a Ch-mass explosion of a C–O WD.

In order to improve on these results, and to verify the consistency between the nebular modelling and the early-time models, we also modelled the nebular spectrum using the abundance tomography approach, see Fig. 6. We extended the density and compositions used in Section 3.2 to verify whether they are compatible and viable at lower velocities. In practice, we modified the abundances at velocities below 6000 km s^{-1}, preserving the density distribution derived through early-time modelling. We find that our stratified model is consistent with the observations, and indeed yields better results than the one-zone model, as expected. We also find, in agreement with the one-zone model, that the stable iron group species are highly abundant in the innermost layers. In fact, they dominate the composition below 5000 km s^{-1}. In particular, stable iron dominates between 3000 and 4500 km s^{-1}, and stable nickel dominates below 2000 km s^{-1}. The total masses we derive were 0.31 M$_\odot$ of ^{56}Ni, 0.27 M$_\odot$ of stable Fe, and 0.08 M$_\odot$ of stable Ni. The total mass of iron group elements is 0.66 M$_\odot$, which is consistent with a moderately luminous SN Ia (Mazzali et al. 2008). Other emission lines produced by the model are the Na I D feature near 5900 Å Ca II] emission near 7200 Å, as well as [Fe II] near 8500 Å, and [Ni II] near 7400 Å. The observed [Ni II] line is somewhat blueshifted relative to its rest wavelength, as noticed in Mazzali et al. (2018). A weak [S II] line is also present near 4000 Å.

5 ABUNDANCE STRATIFICATION

Having produced spectral models of the SNe we now examine their abundances in mass and velocity space.

5.1 SN 2007on

The abundance distribution for the photospheric models of SN 2007on is presented in the top panel of Fig. 7. The oxygen zone dominates down to ∼10 000 km s^{-1}, and the IMEs zone dominates the ejecta down to the lowest photospheric velocity of 3900 km s^{-1}. There is ^{56}Ni located up to ∼12 500 km s^{-1}, but in a much smaller abundance than SN 2011iv. The abundance distribution is what would be expected of a thermonuclear explosion of a WD. It has a chemically layer structure which is consistent with a moderately sub-luminous delayed detonation models of Ch-mass WDs (see e.g. Hoeflich et al. 2017).

It is not clear how the one-component model of the outer layers is connected to the inner two-component model. The problem deviates from 1D, and it would not make sense to reconstruct the abundance distribution in the innermost layers using the standard abundance tomographic approach. However, at early times these inner layers are below the optically thick photosphere; hence, the number of components in the low-velocity layers is not important.

Although the whole abundance distribution of SN 2007on cannot be computed, we can examine the integrated abundance from the early-time models in this work and the nebular phase models from Mazzali et al. (2018). The nebular phase models are sensitive out to 4000 km s^{-1}; therefore, the integrated abundances from this work are used above 4000 km s^{-1}, and those from Mazzali et al. (2018) below this. The abundances are given in Table 3. The total ejecta mass is 1.42 M$_\odot$, with 0.5 M$_\odot$ of unburnt material, 0.61 M$_\odot$ of IMEs, 0.25 M$_\odot$ of ^{56}Ni and 0.06 M$_\odot$ stable nuclear statistical equilibrium (NSE) elements. The ^{56}Ni mass is similar to that derived from the peak of the light curve (Gall et al. 2018).

With the integrated masses obtained from the modelling, the $E_{\rm kin}$ of the explosion can be derived, using the formula

$$E_k = [1.56M(^{56}\mathrm{Ni}) + 1.74M(\mathrm{sNSE}) + 1.24M(\mathrm{IME}) - E_{\rm BE}]10^{51}\ \mathrm{erg} \quad (1)$$

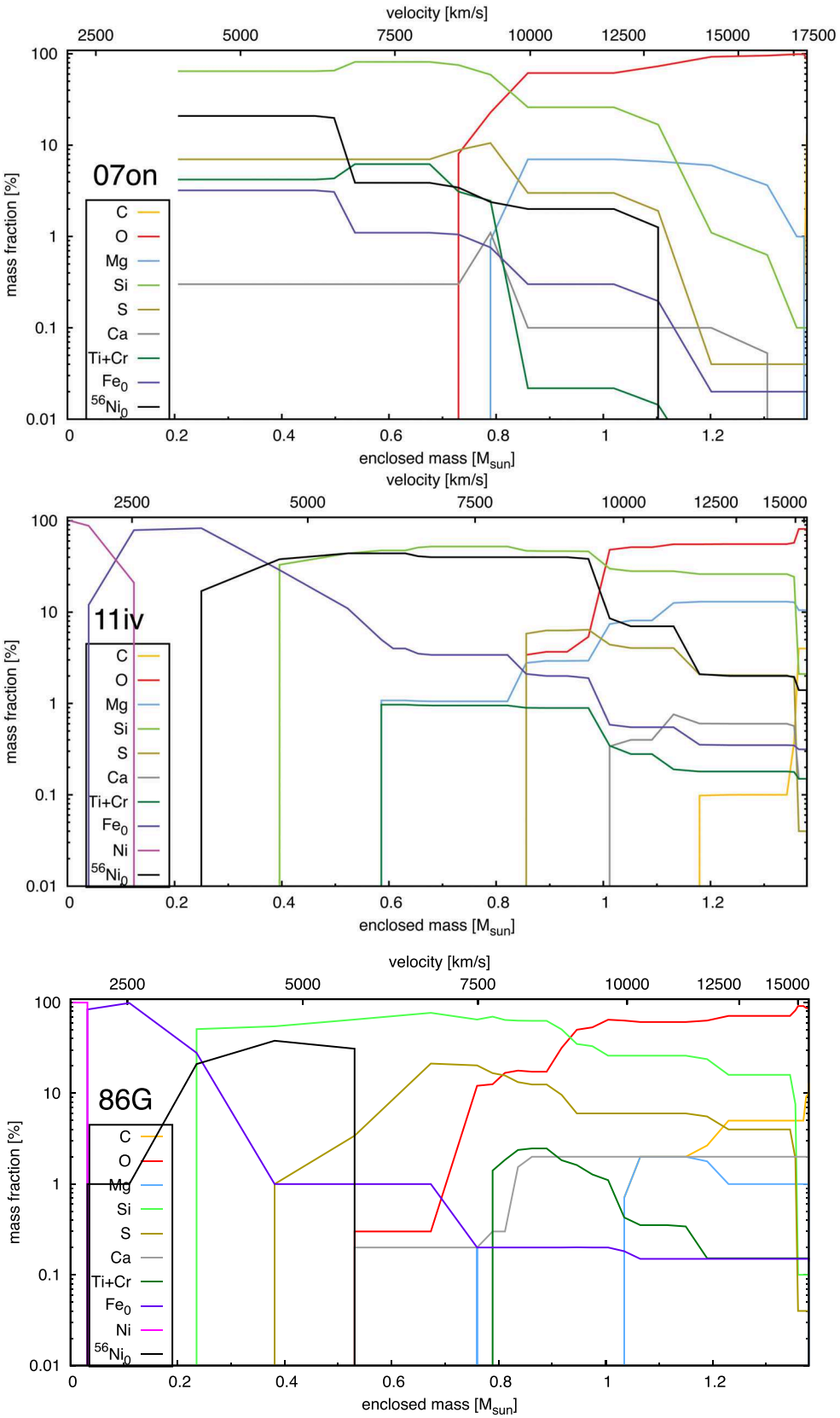

Figure 7. Top: The final abundances of the main elements of SN 2007on derived from spectral modelling, using the W7 density profile. Middle: The final abundances of the main elements of SN 2011iv derived from spectral modelling, using the W7e0.7. Bottom: The abundances of SN 1986G calculated in Ashall et al. (2016). These values were derived using the W7e0.7 density profile. The abundances are given at time $t = 0$ s, $^{56}Ni_0$ denotes the abundance of ^{56}Ni at time $t = 0$ s relative to explosion, and Fe_0 is the stable Fe abundance at $t = 0$ s relative to explosion.

Table 3. The integrated abundances of SN 2007on. The abundances below 4000 km s^{-1} are taken from Mazzali et al. (2018), and the abundances above 4000 km s^{-1} are taken form this work. The errors on the masses are ± 25 per cent.

Material	$v < 4000$ (km s^{-1}) M$_\odot$	$v > 4000$ (km s^{-1}) M$_\odot$	Total M$_\odot$
Unburnt (C+O)[a]	0.00	0.50	0.50
IME	0.01	0.60	0.61
^{56}Ni	0.17	0.08	0.25
stable NSE	0.02	0.04	0.06
Total	0.2	1.22	1.42

[a] Some of this oxygen will have been produced through burning.

(Woosley et al. 2007), where $E_{\rm BE}$ is the binding energy of the progenitor WD, $M(^{56}{\rm Ni})$ is the ^{56}Ni mass, M(sNSE) is the mass of stable NSE elements, and M(IME) is the total IME mass in the ejecta. For a standard energy explosion of Ch-mass WD, $E_{\rm BE} = 0.46 \times 10^{51}$ erg.

Using equation (1), a $E_{\rm kin}$ of $(1.24 - E_{BE}) \times 10^{51}$ erg is obtained, where $E_{\rm BE}$ varies depending on the explosion scenario. If the normal $E_{\rm BE} = 0.46\times\ 10^{51}$ erg is used, a total $E_{\rm kin} = 0.78\times\ 10^{51}$ erg is obtained, which is inconsistent with the input model with $1.3\times\ 10^{51}$ erg. To achieve a much lower $E_{\rm BE}$ requires a low ρ_c. A low ρ_c is in line with the nebular spectral models (see Mazzali et al. 2018), which show that SN 2007on had a low mass of stable NSE elements (0.06 M$_\odot$)[9]. This is much lower than other SNe Ia (see Stehle et al. (2005); Ashall et al. (2016)). It is not apparent whether a Ch-mass WD can produce such a low mass of stable NSE elements. In the collision scenario of two 0.7 M$_\odot$ WDs, the ρ_c and $E_{\rm BE}$ will be lower. $E_{\rm BE}$ for a non-rotating WD with mass 0.7 M$_\odot$ is $0.02\times\ 10^{51}$ erg (Yoon & Langer 2005). Therefore, the collision scenario gives consistency between the $E_{\rm kin}$ ($1.2\times\ 10^{51}$ erg) calculated from the nucleosynthesis yield and the $E_{\rm kin}$ calculated with the input density profile ($1.3\times\ 10^{51}$ erg).

As noted previously, SN 2007on shows two late-time nebular components, both of these components have a similar ejecta mass ∼0.1 M$_\odot$ and a similar ^{56}Ni mass of ∼0.085 M$_\odot$, but a different ionization state caused by different amounts of stable NSE elements, which act as coolants. Two of the scenarios that could produce two late-time components. These are the collision of two WDs or an off-centre ignition of a WD in the delayed denotation scenario.

In an off-centre ignition scenario, the detonation phase starts away from the centre of the WD, which causes a 'ring'-like structure of ^{56}Ni around the central core, with a 'blob' of ^{56}Ni where detonation started (see e.g. Fesen et al. 2007). Within the delayed detonation scenario, ^{56}Ni is produced during both the deflagration and detonation burning phases. As we will discuss in Section 7, the production is dominated by the detonation phase in normal-bright SNe Ia and by the deflagration phase in sub-luminous objects. For the transitional SNe Ia such as SN 2007on and SN 2011iv, the best-fitting delayed detonation models produce about equal amounts of ^{56}Ni in each phase, and the point of detonation occurs at ∼7000 km s^{-1} (see Gall et al. 2018). The corresponding off-centre 2D simulation has been applied to S-Andromeda and it was found that a similar amount of ^{56}Ni was produced in each phase, and off-set with an average velocity of 6000 km s^{-1} (Fesen et al. 2007). Detailed tuning of parameters is beyond the scope of this study, but results in the literature make off-centre delayed detonations a viable option because components with similar amount of ^{56}Ni and a slightly larger separation have been seen.

The abundance distribution of the outer layers of SN 2007on is not in disagreement with an off-centre explosion; however, most signatures of an off-centre explosion can be seen in the nebular phase and we cannot draw any strong conclusions on this with just the early-time data. For a more detailed discussion, see Mazzali et al. (2018). Other aspects, such as the colour curve and the light curve, of SN 2007on also match the delayed denotation scenario (Hoeflich et al. 2017; Gall et al. 2018).

However, the two things that it seems cannot be explained by the delayed denotation scenario are the lack of stable NSE elements produced in the ejecta (i.e. can a single Ch-mass WD have a low enough ρ_c to produce the very small abundance of stable NSE elements seen in SN 2007on?) and the similar ejecta masses of each nebula component. The collision of two ∼0.7 M$_\odot$ WDs can explain the lack of stable NSE elements, due to the lower ρ_c. It also naturally explains the equal mass of each nebula. Additionally, ∼0.7 M$_\odot$ is the typical mass of WD in the Universe (Kepler et al. 2017). The collisions of two WDs are likely to be rare, explaining why only a few SNe Ia have been claimed to have double-peaked nebular lines (Dong et al. 2015).

5.2 SN 2011iv

The abundance distribution of SN 2011iv as a function of mass and velocity has been reconstructed (see the middle panel in Fig. 7). The nucleosynthesis follows what would be expected of a thermonuclear runaway reaction. However, the unburnt and IME zones are much larger in SN 2011iv than in a more luminous SN such as SN 2011fe. This indicates that the burning was less efficient. The oxygen zone dominates down to ∼9500 km s^{-1}, and there are signs of a small amount (< 1 per cent) of carbon in the outermost layers. The abundance distribution indicates that there is mixing in the ejecta, with ^{56}Ni and Ti+Cr located in the outermost velocities (>15 000 km s^{-1}). The IME zone dominates from 9500 km s^{-1} down to 6000 km s^{-1}, and the inner-most layers, below 6000 km s^{-1}, mainly consist of NSE elements.

As discussed in Section 3.2.5, an SN Ia with a large progenitor metallicity will have a lower Y_e in the outer layers. This low Y_e provides a large ^{54}Fe production in these high-velocity layers. Usually, the Fe production also decreases in intermediate velocity layers and peaks in abundance in the central densest regions. In SN 2011iv there is a larger than average Fe abundance in the outer layers, which has been linked back to the progenitor metallicity (see Section 3.2.5). However, there is not a decreasing Fe abundance in the intermediate velocity regions (see Fig. 7). In the companion paper (Mazzali et al. 2018), it was found that SN 2011iv could have come from an off-centre ignition of a WD. Therefore, we speculate that the increase in Fe abundance in the intermediate-velocity regions is caused by the off-centre ignition of the WD.

The final integrated abundances are presented in Table 4. SN 2011iv produced 0.24 M$_\odot$ of unburnt (C+O) material, 0.48 M$_\odot$ of IMEs, 0.35 M$_\odot$ of stable NSE, and 0.31 M$_\odot$ of ^{56}Ni. This is in line with the two-component models of Mazzali et al. (2018) that find that SN 2011iv has 0.32 M$_\odot$ of ^{56}Ni. Putting the integrated masses obtained from the modelling into equation (1), the kinetic energy of SN 2011iv calculated from the abundances ($1.2 \pm 0.3 \times 10^{51}$ erg)[10] is similar to the $E_{\rm kin}$ of the input density

[9] A low ρ_c implies a low electron capture rate and pushes burning away from stable NSE elements.

[10] For a low-energy explosion of Ch-mass WD $E_{BE} = 0.49 \times 10^{51}$ erg.

Table 4. Integrated abundances from the full abundance tomography modelling of SN 2011iv. The errors on the masses are ±25 per cent.

Element	W7e0.7 $M_\odot$
C	<0.01
O	0.24
Mg	0.05
Si	0.39
S	0.03
Ca	0.01
Ti+Cr	<0.01
Fe	0.27
^{56}Ni	0.31
Ni	0.08
M_{tot}	1.38

profile, W7e0.7 ($0.9 \pm 0.2 \times 10^{51}$ erg). Given the error on the abundances and E_{kin} of the density profile, there is good consistency between the E_{kin} derived through abundances and the E_{kin} obtained from the input density profile. We note that the ^{56}Ni mass ratio (0.81) of SN 2007on to SN 2011iv (0.25/0.31 $M_\odot$) obtained in this work is remarkably similar to that derived from the delayed detonation models used in Hoeflich et al. (2017) and in appendix D of Gall et al. (2018) who obtain a ratio of 0.86 (0.32 $M_\odot$/0.37 $M_\odot$). The absolute difference in ^{56}Ni masses is due to the slightly larger distance modulus used in Hoeflich et al. (2017) (see Section 2).

The abundance distribution indicates that SN 2011iv was consistent with a Ch-mass delayed detonation explosion of a C–O WD. In this scenario, the explosion had a low deflagration to detonation ρ_{tr}, which caused the WD to partially unbind and the burning in the detonation phase to be less efficient, producing more IMEs. The fact that there is ^{56}Ni located further out in the ejecta indicates that there was some mixing, possibly during the deflagration phase. The lack of ^{56}Ni below 2500 km s^{-1} is in line with explosion models. A higher ρ_c will increase the electron capture rate and produce stable NSE elements in the innermost layers (Hoeflich et al. 2017). As the ^{56}Ni is located further out in the ejecta the mean free path of the photons will be longer, causing the rise of the SN light curve to be faster, which matches the observations. These results add to the growing evidence that the ρ_c of SN 2011iv was higher than standard SNe Ia. The results of this abundance distribution plot also complement the results of Mazzali et al. (2018) who determine that SN 2011iv was an off-centre explosion.

5.3 Comparison of abundance stratification

In delayed detonation explosion models fainter SNe Ia have a smaller ρ_{tr} and a longer deflagration phase, which results in greater pre-expansion during deflagration and less effective burning during detonation, thus producing less ^{56}Ni. The abundance stratification of three transitional SNe Ia (SNe 2007on, 2011iv, and 1986G) is presented in Fig. 7. If the results of these SNe Ia are interpreted in terms of delayed denotation explosions, SN 2011iv synthesized the most ^{56}Ni (0.31 $M_\odot$) and therefore had the largest ρ_{tr}. The pre-expansion during the deflagration phase partially unbound the WD; therefore, the burning during the detonation phase was less effective than in a normal SN Ia. SN 2007on had a ρ_{tr} between that of SN 2011iv and SN 1986G. SN 2007on had a longer deflagration phase than SN 2011iv, which further unbound the WD producing less effective burning during the detonation. Hence, SN 2007on synthesized an intermediate amount of ^{56}Ni. SN 1986G had the lowest ρ_{tr} and produced the least amount of ^{56}Ni with virtually none being located at high velocity. However, this picture does not take second-order parameters such as ρ_c of the WD into account.

In fact in the delayed detonation scenario, SNe 1986G and 2011iv can be thought of as very similar explosions, with different ρ_{tr}. SN 1986G had lower photospheric velocities, a larger abundance of unburnt material (0.34 $M_\odot$), and a E_{kin} of $1.0 \pm 0.2 \times 10^{51}$ erg[11]. On the other hand, SN 2011iv had larger photospheric velocities, a smaller abundance of unburnt material (0.24 $M_\odot$), and a E_{kin} of $1.2 \pm 0.3 \times 10^{51}$ erg[11]. In the less luminous SN 1986G more oxygen and carbon remained unburnt and did not contribute to the energy production; hence, the v_{ph} and E_{kin} were lower. More similarities between both SNe are the facts that their models favoured the same density profile, they both had a high ρ_c, as well as an off-centre ^{56}Ni distribution. This is evidence that SNe 2011iv and 1986G came from very similar progenitor systems.

It may actually be the case that SNe 2007on and 1986G were also similar explosions. The total mass of Fe-group elements for SN 2007on was 0.31 $M_\odot$ and for SN 1986G was 0.34 $M_\odot$. In the delayed detonation scenario, this indicates that their ρ_{tr} were similar, but that ρ_c is the main difference between these objects. The high ρ_c in SN 1986G increases the amount of stable NSE elements produced at the expense of ^{56}Ni. Therefore, we have a situation where SN 2011iv and SN 1986G have similar ρ_c and different ρ_{tr}, but SN 2007on and SN 1986G have different ρ_c and similar ρ_{tr}. This suggests that they may all come from a similar progenitor scenario, and accounting for both parameters (ρ_c and ρ_{tr}) is important if these transitional SNe Ia are to be used as distance indicators.

However, comparing these objects in terms of just ρ_{tr} and ρ_c is an over simplification. There could be other factors that differ between them, including the points of ignition. Mazzali et al. (2018) demonstrated that SN 2011iv had an off-centre ignition, whereas Ashall et al. (2016) found no evidence for SN 1986G igniting off-centre. It could also be the case that SN 2007on had an extremely off-centre ignition, and it should be noted that the outer layers of SN 2007on are consistent with a delayed detonation Ch-mass explosion, although the collision of two WDs with a total ejecta mass near the Ch-mass is also a viable scenario (Mazzali et al. 2018).

6 BOLOMETRIC LIGHT CURVES

In the spirit of abundance tomography, we built a bolometric light curve to test whether the model of SN 2011iv may be compatible with the observations. The light curve was based on the density and abundance distributions derived above. We used a well-tested Montecarlo code, which starts with the same description of gamma-ray and positron emission/deposition as in the nebular phase code, and follows optical photons as they propagate through the SN ejecta using the grey approximation. The code was first described by Cappellaro et al. (1997), then improved upon by Mazzali (2000), and it has been used several times in the study of both SNe Ia (e.g. Ashall et al. 2016) and SNe Ib/c (e.g. Mazzali et al. 2014).

The synthetic light curve (see Fig. 8) reaches maximum light ∼18 d after explosion at M (Bol)$_{Max}$ ∼ −18.6 mag, or $\log(L) = 42.91$ erg cm^{-2} s^{-1}. It matches the observed light curve very well both around peak and in the early decline phase, up to about day 40. Thereafter, the observed light curve declines more

[11] E_{kin} calculated from integrated abundances.

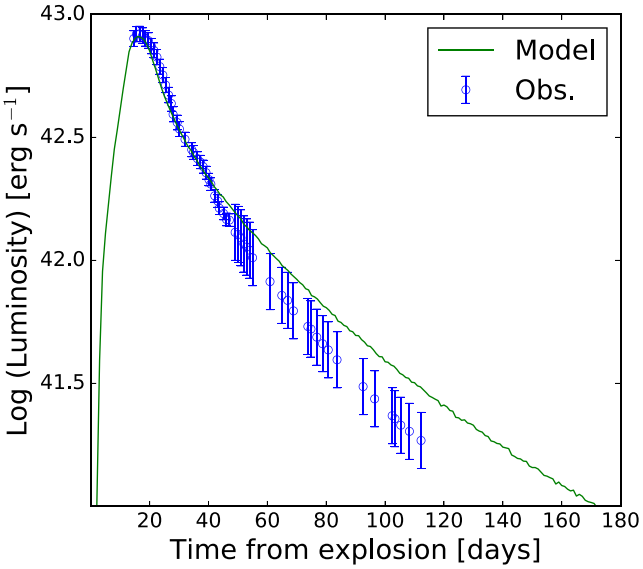

Figure 8. The observed (blue) and modelled (green) bolometric light curve of SN 2011iv. The observed bolometric light curve of SN 2011iv was taken from Gall et al. (2018), and constructed using SNOOPY (Burns et al. 2011, 2014). The near-IR photometric coverage of SN 2011iv after 40 d past maximum light was poor; hence, we adopted a standard flux error after this point of 30 per cent, which could be this missing contribution (see Gall et al. 2018, fig. 11). There could also be up to 10 per cent flux in the MIR at these epochs.

rapidly. As the light curve also reproduces the observations at day 270 (this is by definition as the same code that is used to compute the light curve is used to compute the deposition for the nebular spectrum), due to a lack of data, it may be possible that the near-infrared and mid-infrared flux is not properly accounted for in the construction of the pseudo-bolometric light curve.

7 PROPERTIES OF TRANSITIONAL SNE IA MODELS

One issue when comparing transitional and sub-luminous SNe Ia is the degeneracy in $\Delta m_{15}(B)$ (Phillips 2012; Burns et al. 2014; Gall et al. 2018). SNe Ia with $\Delta m_{15}(B) > 1.7$ mag suffer from the fact that two SNe Ia with different light-curve shapes can have the same value of $\Delta m_{15}(B)$. As opacity is the main driver of SN Ia early-time light-curve shape (Mazzali et al. 2007), fainter SNe Ia have faster light curves than standard SNe Ia. This is because line opacity dominates in SNe Ia (Pauldrach et al. 1996), and Fe-group elements contribute to the opacity by a factor of 10 more than IMEs. Therefore, an SN Ia with a smaller ^{56}Ni mass will have a low opacity and a fast evolving light curve (as ^{56}Ni decays to ^{56}Co and ^{56}Fe). In the most extreme cases, the least luminous SNe Ia, with very little ^{56}Ni, reach the ^{56}Co decay tail in the light curve before 15 d past B-band maximum. Therefore, objects such as SN 2005ke and SN 2006mr would be directly comparable if just $\Delta m_{15}(B)$ was used. Burns et al. (2014) proposed a new method of characterizing light curve shapes. This is the colour-stretch parameter, s_{BV}. It is a dimensionless parameter defined to be the time difference between B-band maximum and the epoch the $B - V$ colour reaches its maximum value, divided by 30 d. Ordering fast declining SNe Ia by s_{BV} breaks this degeneracy and places the SNe in order of peak luminosity, but it does not alter the fact there is still some variation between fast-declining SNe Ia. For example, SN 2011iv sits above the s_{BV} versus M_B relation, and it does not answer the question why does SN 2007on show double-peaked emission in the nebular phase. SNe 2007on and 2011iv have s_{BV} values of 0.57 ± 0.01 and 0.64 ± 0.01, respectively (Gall et al. 2018).

Having examined two transitional SNe Ia in detail we now look at the general properties of transitional and sub-luminous SNe Ia. It has been suggested that sub-luminous SNe Ia could come from multiple progenitor scenarios, and could be a totally different class of explosion when compared to normal and transitional SNe Ia (see e.g. Iben & Tutukov 1984; Mazzali et al. 2008; Sim et al. 2010; Blondin et al. 2017; Jiang et al. 2017). Furthermore, it has been claimed by some that SNe Ia with $\Delta m_{15}(B)$>1.4 mag can only be produced by sub-Ch-mass explosions, and not by delayed detonation explosions (Blondin et al. 2017). Here, we address the evidence for this at the faint end of the luminosity width relation and examine how the progenitors of transitional SNe Ia link to those of normal and sub-luminous SNe Ia. To do this, we examine six SNe Ia (from most to least luminous: SNe 2004eo, 2003hv, 2011iv, 2007on, 1986G, 1991bg) that have extensive and accurate data sets and that have been studied in detail through spectral modelling. These SNe vary in s_{BV} between 0.81 and 0.38. Table 5 shows the basic properties of each SN, as well as their suggested explosion scenario, and Fig. 9 shows the maximum light and nebular phase spectra and models of these SNe.

SN 2004eo is on the faint end of the normal SNe Ia population; it was consistent with a Ch-mass delayed detonation explosion that produced 0.43 $M_\odot$ of ^{56}Ni (Mazzali et al. 2008). Moving down in luminosity, SN 2003hv had an early-time evolution between that of SNe 2004eo and 2011iv. Optical nebular phase modelling found that SN 2003hv's high [Fe III] to [Fe II] ratio was caused by a lower ρ_c, and less recombination than a standard SNe Ia (Mazzali et al. 2011). This is in line with density profiles of sub-Ch-mass models that have an ejecta mass of $\sim$1.2 $M_\odot$. However, mid-infrared observations indicate that SN 2003hv shows signs of asymmetry (Gerardy et al. 2007). Motohara et al. (2006) show that, at +394 d relative to B-band maximum, the 1.257 and 1.644 μm [Fe II] features had a pot-bellied profile shape (see Stritzinger et al. 2015, fig. 13 for details). This indicates an off-centre explosion, and that the highest density burning in this SN took place quite far away from the centre of the progenitor star, implying that SN 2003hv could have been a low central density, delayed detonation Ch-mass explosion.

SN 2011iv had an s_{BV} of 0.65 and produced fits that are in line with a delayed detonation explosion, which had a higher ρ_c and a lower ρ_{tr} than a standard SNe Ia. It is possible that SN 2011iv had an off-centre ignition (Mazzali et al. 2018). The next SN in the sequence is SN 2007on. This SN deviates from the standard explosion model, as is seen from its double-peaked nebular lines. These double peaks possibly come from two separate nebular components (Mazzali et al. 2018), indicating the SN could have come from a Ch-mass off-centre ignition delayed detonation explosion with a low ρ_c, or the collision of two roughly equal mass WDs. SN 1986G has been studied in detail by Ashall et al. (2016). This SN is of particular interest, as it is one of the few SN Ia that has an early-time, intermediate Ti II absorption feature at 4500 Å. It also has an ^{56}Ni mass between SN 2007on and SN 1991bg. SN 1986G was compatible with a low-energy (high ρ_c) delayed detonation Ch-mass explosion.

Finally, we turn to SN 1991bg, the least luminous object in our sample. It produced $\sim$0.1 $M_\odot$ of ^{56}Ni, and was theorized to be a merger of two WDs (Mazzali & Hachinger 2012), a sub-Ch-mass explosion (Sim et al. 2010; Blondin et al. 2017), or a Ch-mass delayed detonation explosion (Höflich et al. 2002). Blondin et al. (2017) argue that classical delayed detonation models can only

Table 5. The main properties of six SNe Ia including normal (SN 2004eo), transitional (SN 1986G, SN 2003hv, SN 2007on, SN 2011iv), and sub-luminous (SN 1991bg) SNe Ia. All of the SN in the table have been spectroscopically modelled, and the ^{56}Ni mass was derived from spectral modelling. The SNe are ordered in luminosity. Table references: (1) Mazzali et al. (2008), (2) Mazzali et al. (2011), (3) This paper, (4) Ashall et al. (2016), (5) Mazzali & Hachinger (2012).

SN	s_{BV}	$\Delta m_{15}(B)$ (mag)	Bol $L_{\max}$ (10^{43}erg)	^{56}Ni ($M_\odot$)	Explosion	M_{ej} ($M_\odot$)	Host type	Observational properties	Ref.
2004eo	0.81	1.46	1.15	0.43	DDT[a]	∼1.38	SB	Normal SNe Ia	1
2003hv	0.75	1.61	1.00	0.2–0.4[b]	sub Ch det./DDT[c]	∼1.2/1.38	E/S0	High [Fe II] to [Fe III] ratio	2
2011iv	0.65	1.77	0.87	0.31	DDT[a, c, d]	∼1.38	E	Luminous for LC shape	3
2007on	0.58	1.96	0.54	0.25	Collision/DDT[a, b]	1.42/1.38	E	Double peak nebular lines	3
1986G	0.54	1.81	0.4	0.14	DDT[a, e]	∼1.38	S0-pec	Intermediate Ti II absorption	4
1991bg	0.38	1.98	0.26	0.1	Merger/DDT[a]	∼1.2–1.38	E	Rapid ionization change[f]	5

[a]Delayed detonation.
[b]Dependent on rise time assumed.
[c]Off-centre detonation.
[d] ^{56}Ni made in deflagration phase.
[e]No ^{56}Ni made in deflagration phase.
[f]In the nebular phase.

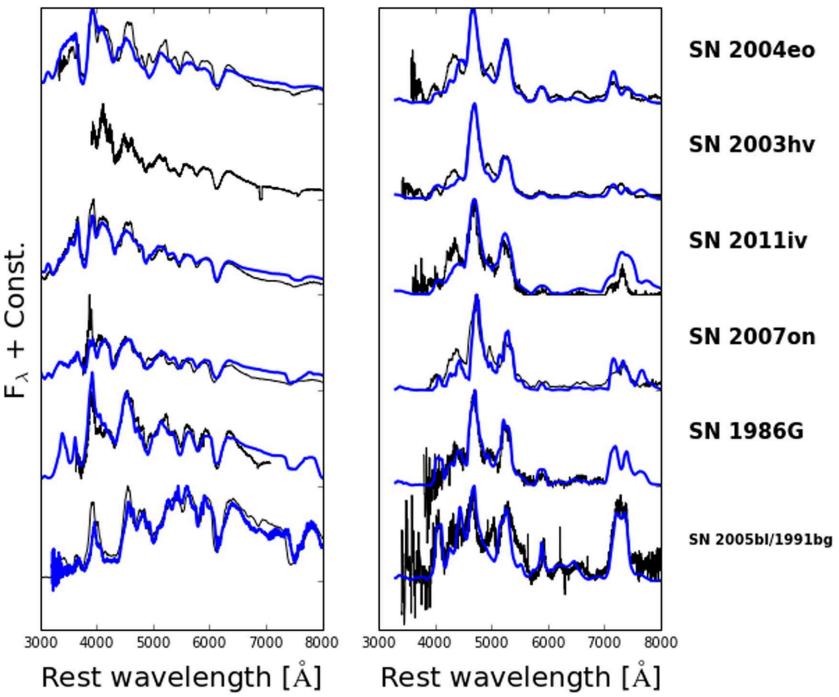

Figure 9. Left: Maximum light spectra (black) and models (blue) of the SNe in Table 5. No models have been made for the early time of SN 2003hv or SN 1991bg. Instead of SN 1991bg, we plot SN 2005bl (Hachinger et al. 2009) that is a similar SN. Right: Nebular phase spectra (black) and models (blue) of the same SNe.

follow the luminosity width relation at values of $\Delta m_{15}(B) < 1.38$ mag. Further down the relation their theoretical models take a sharp orthogonal-like turn that produces an 'antirelation'. A similar anticorrelation was found by Pinto & Eastman (2000a), but was subsequently corrected in Pinto & Eastman (2000b). Overall Hoeflich et al. (2017) demonstrated that the sub-Ch-mass explosions, or merger models do not correctly reproduce the whole evolution of sub-luminous SNe, whilst delayed detonation models can. Höflich et al. (2002) argue that SN 1999by (a 1991bg-like SN) can be explained by a delayed detonation scenario. However, Blondin, Dessart & Hillier (2018) claim the opposite result, and that SN 1999by can only be produced with a sub-Ch-mass explosion. It should be noted that the models from Blondin et al. (2018) are too red with respect to the observations and produce no carbon feature at maximum light. Furthermore, their models predict a $\Delta m_{15}(B)$ of 1.64 mag, which is considerably different from the measured value of $\Delta m_{15}(B) = 1.90$ mag (Garnavich et al. 2004). On the other hand, SN 1991bg models do require a decrease in density in the inner most region of the ejecta to explain the rapid ionization change in the nebular phase (Mazzali & Hachinger 2012), and this is not consistent with delayed detonation model predictions.

7.1 s_{BV} versus $L_{\max}$ relation

It is apparent that most transitional and sub-luminous SNe Ia can be modelled by Ch-mass delayed detonation explosions, but this does not rule out other progenitor or explosion scenarios. Regardless of

the nature of these explosions, the observational properties of SNe Ia at the faint end of the luminosity width relation are diverse.

The s_{BV} parameter has allowed the area of fast declining SNe Ia to be reassessed. Recently, it has been suggested that some sub-luminous objects come from a distinct population compared to normal SNe Ia. By examining s_{BV} versus bolometric maximum light luminosity ($L_{\rm max}$), Dhawan et al. (2017) determined that 6 out of 24 SNe Ia came from a different class of explosions. These SNe Ia were the least luminous in the sample, had no near-infrared secondary maximum, and had a near-infrared primary maximum after the time of B-band maximum. Whereas normal SNe Ia have two near-infrared maxima, one before B-band maximum and one after B-band maximum. Typically, observations show that as the luminosity of SNe Ia decreases the time of secondary maximum gets closer to the time of B-band maximum, except for the least luminous SNe Ia that show one near-infrared maximum after the time of B-band maximum (Phillips 2012).

We examine the evidence for two populations of sub-luminous SNe Ia with our models and results. To do this we take 24 SNe Ia from the CSP and compute their bolometric light curves to obtain $L_{\rm max}$. The bolometric light curves are constructed from the CSP data using all available filters: *ugriBVYJH*. Since the photometry are not all coincident, we must first fit interpolating functions to the observed data. In order to capture the uncertainty in the interpolation process, we use Gaussian Processes (GP; Rasmussen & Williams 2006) with a Matern kernel. The mean function is taken to be the best fit from SNooPy (Burns et al. 2011, 2014), with a linear extrapolation at late times if data exist beyond the extent of the template. This not only allows for a robust fit of the light curves but also captures the diversity in the light-curve shapes from SN to SN.

With the measured and interpolated fluxes, we multiply the Hsiao et al. (2007) spectral energy distribution (SED) with a basis spline and tune the spline coefficients until synthetic photometry from the SED matches the observed colours. Using the methods from Burns et al. (2014), we estimate the extinction due to both Milky Way and host galaxy dust. The warped SED is then de-reddened using the Fitzpatrick (1999) reddening law. Finally, the warped, de-reddened SED is integrated from λ_u to λ_H to get the bolometric flux. The bolometric flux is converted into a bolometric luminosity assuming a Hubble distance with $H_0 = 70\,{\rm km\,s^{-1}\,Mpc^{-1}}$, or using an independent distance estimate for nearby SNe (see Table C1).

To determine uncertainties in $L_{\rm bol}$, we take a Monte carlo approach. We draw 100 random realizations from the Gaussian Process interpolators and 100 random extinctions consistent with the observed colours and compute 100 values of the bolometric light curve. This simulates the propagation of correlated errors from both the interpolating in time (GPs) and in wavelength (de-reddening) to the bolometric flux. We find the errors due to extinction and distance to be the most important. A spline function is fitted to the bolometric light curves to obtain the bolometric maximum, $L_{\rm max}$, for each MC iteration. The median and standard deviation of the bolometric maximum from the 100 MC iterations is used as the final bolometric maximum and its associated error. Table C1 presents the properties and values of the 24 SNe analysed.

The top left-hand panel in Fig. 10 shows s_{BV} versus $L_{\rm max}$ for the 24 CSP SNe Ia we have analysed, and 7 SNe Ia that were modelled using the abundance tomographic approach. From the CSP data alone, we find no objects in the area of parameter space (i.e. $0.45 < s_{BV} < 0.6$) between the least luminous and 'normal' SNe Ia populations. However, from the abundance stratification models, we find that SN 1986G sits in the area of parameter space between the two populations and acts as a link between normal and sub-luminous SNe Ia. This is where one would expect SN 1986G to be located, as it is the only SNe Ia that had an intermediate Ti II absorption feature. Furthermore, SN 1986G had a secondary near-infrared maximum 10 ± 5 d[12] after B-band maximum (Frogel et al. 1987). This is significantly shorter than the time of secondary near-infrared maximum of other SNe Ia. For example, the second near-infrared maximum of SN 2007on occurred 20 d after B-band maximum. However, due to its large host galaxy extinction, the position of SN 1986G on this plot is very uncertain. It is apparent from Fig. 10 that these connecting 1986G-like SNe are rare. Another SN that could possibly be a connection between these two populations is SN 2007ba. Spectroscopically, it was classified as a 1991bg-like SN, it had strong Ti II absorption at maximum light, and a near-infrared secondary maximum, but the time of Y-band maximum was after the time of B-band maximum. This is not the case for the other normal SNe Ia. It should also be noted that the host galaxy extinction calculated for SN 2007ba in Burns et al. (2014) is too large and incompatible with its spectral shape. In fact, the spectra of SN 2007ba indicate that the SN is consistent with almost no host galaxy extinction. The likely reason for this incorrect value of extinction is because it was assumed that there was a single intrinsic colour–s_{BV} relation for SNe Ia. However, according to theoretical models for fast declining SNe Ia, there should be a variation in colour, caused by different ρ_c, for the same s_{BV}.

To examine the s_{BV} versus $L_{\rm max}$ relation further we turn our attention to the delayed detonation models of Hoeflich et al. (2017) (see Table C2). The model light curves are based on time-dependent non-LTE simulations, as described in Hoeflich, Khokhlov & Wheeler (1995), Höflich et al. (2002), Höflich (2003a), Höflich (2003b), and references there in. The models were upgraded by atomic models subsequently. They are Ch-mass explosions of C–O WDs. After an initial deflagration phase, a detonation is triggered when the flame front drops to a $\rho_{\rm tr}$. For a normal bright SNe Ia, to first order, the $\rho_{\rm tr}$ determines the amount of ^{56}Ni synthesized in the ejecta, as there is more effective burning during the detonation. Hence, $\rho_{\rm tr}$ is the main driver in the luminosity–width relation (Höflich et al. 2002). However, some second-order parameters that can affect the evolution of the explosion are the primordial metallicity of the progenitor star, the size of the accompanying main sequence star, and the ρ_c of the WD. Here, we will just focus on $\rho_{\rm tr}$ and $\rho_{\rm c}$.

Comparing the models of Hoeflich et al. (2017) to the CSP data, we find a very similar trend. In the top right-hand panel of Fig. 10, we present a suite of models with the same central density ($2 \times 10^9\,{\rm g\,cm^{-3}}$), solar metallicity, and main-sequence mass of $5\,{\rm M_\odot}$, but varying $\rho_{\rm tr}$. To first order it is clear that varying $\rho_{\rm tr}$ produces the same trend as the observations. The sudden drop in luminosity at $s_{BV} = 0.4$–0.6 corresponds to the $\Delta m_{15}(B)$'cliff'. The $\Delta m_{15}(B)$'cliff' is seen as a rapid drop in brightness at $\Delta m_{15}(B) > 1.5$ mag, it is caused by the transition from doubly to singly ionized iron group elements that allows SNe to enter a regime of quickly dropping opacity (for more discussion, see Hoeflich et al. 2017). In these models, the least luminous SNe show only one near-infrared maximum (which peaks after B-band maximum), whereas the more luminous models show two near-infrared maxima (one peaks before B-band maximum and one after). This is because the secondary peak is related to the phase of the shrinking photospheric radius (Hoflich et al. 1995). Therefore, the secondary peak is later as brightness increases. In the sub-luminous regime, the first and second peaks appear to merge and show one very broad peak. This broad peak is

[12] Generous errors are given due to the age of the photometry.

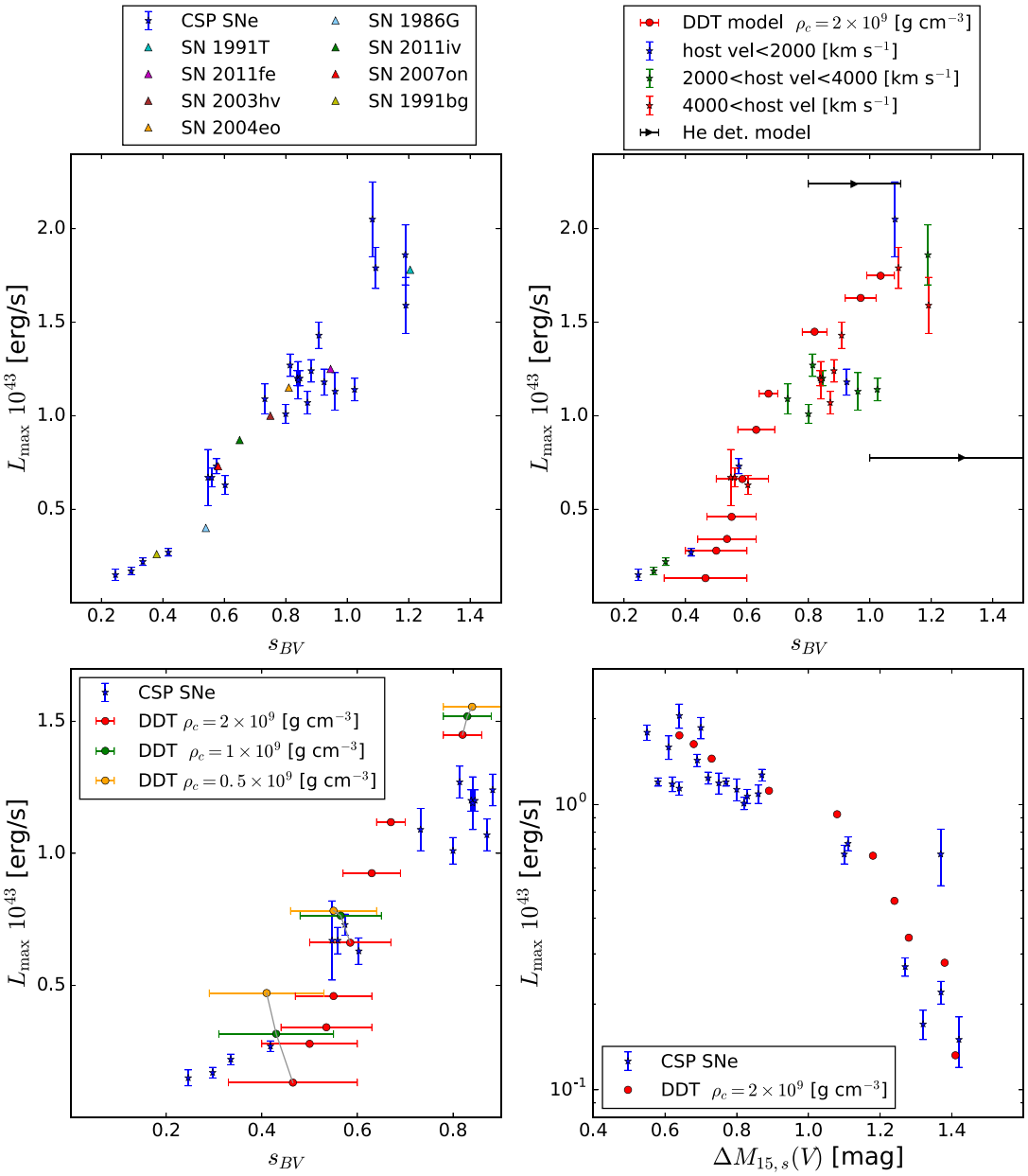

Figure 10. Top left: s_{BV} versus $L_{\rm max}$ relation for the 24 CSP SNe Ia (blue stars), and 8 SNe modelled through abundance tomography (triangles). Top right: s_{BV} versus $L_{\rm max}$ relation for the same 24 CSP SNe (stars) and explosion models. The SNe are separated in colour depending on the velocity of their host galaxy. The bins correspond to SNe that were in galaxies with velocities less than 2000 km s^{-1}(red), with velocities between 2000 and 4000 km s^{-1}(green), and with velocities greater than 4000 km s^{-1}(orange). The red circles are delayed detonation models with the same initial properties but varying $\rho_{\rm tr}$, and the black triangles and He detonation models. Bottom left: The same as the top right-hand panel but zoomed on the sub-luminous section, delayed detonation models with different $\rho_{\rm c}$ $1\times$ 10^9 g cm^{-3} (green circle) and $0.5\times$ 10^9 g cm^{-3}(orange circle) are also plotted. The grey solid line connects models that have the same $\rho_{\rm tr}$. Bottom right: $\Delta M_{15,\,s}(V)$ versus $L_{\rm max}$ for comparison, $\Delta M_{15,\,s}(V)$ is the preferred measurement of the light curve in Hoeflich et al. (2017). Note that the errors on the observations do not include errors on the distances (see Table C1). The errors in the theoretical s_{BV} measurement are caused by a jitter in B and V due to the spatial discretization of the models and uncertainties in the atomic models, in particular during the phase of the Lira relation, as discussed in Hoeflich et al. (2017).

always at a later epoch when compared to the first peak in the more luminous models. For comparison, we also plot two He detonation models from Hoeflich et al. (2017) that appear not to match the observations. We emphasize that the models presented here were not tuned to fit the data, and all models were chosen from previously published work.

For normal SNe Ia, 10–20 per cent of ^{56}Ni can be made in the deflagration phase, where some high-density deflagration burning is required for the pre-expansion to agree with observations. These densities are high enough to reach NSE, and when the densities exceed $\sim$10^9 g cm^{-3} it can cause a shift in the NSE away from ^{56}Ni towards stable NSE elements due to the increased electron capture

rate (Hoeflich et al. 2017). Hence, the amount of ^{56}Ni produced during the deflagration phase is dependent on ρ_c. For sub-luminous SNe Ia deflagration burning dominates and most of the ^{56}Ni is produced during this phase. Therefore, the ρ_c of sub-luminous SNe Ia has a large effect on its luminosity. In fact, a change of $\rho_c = 1 \times 10^9$ g cm^{-3} to 2×10^9 g cm^{-3} can change the ^{56}Ni mass by a factor of 2, which could explain some of the difference between SN 1986G and SN 2007on. Generally, an SN Ia with a high ρ_c will not have ^{56}Ni in the inner most layers, it will be located further out in the ejecta (Hoeflich et al. 2017), as is seen in the abundance stratification models of SN 2011iv and SN 1986G (see Fig. 7). The bottom left-hand panel in Fig. 10 is similar to the top right-hand panel but with delayed detonation models that have different ρ_c. As discussed above, changing the ρ_c has the biggest effect on the least luminous models.

It is evident from the explosion and spectral models that SNe Ia can be produced through the delayed detonation scenario for almost the whole range of observations. However, in nature we do not see a smooth distribution of SNe Ia properties. There is a bimodal distribution in $L_{\rm max}$, with a lack of SNe Ia connecting sub-luminous and normal SNe Ia. The increased number of objects at the faint end of the distribution could be due to multiple progenitor scenarios (delayed detonation explosions, small amplitude PDDs, mergers and sub Ch-mass explosion). There is clearly a lack of SNe in the region between normal and sub-luminous SNe Ia, and it is likely to be intrinsic as only a handful of these objects have ever been discovered and followed. [13] This region corresponds to a $\rho_{\rm tr} = \sim$12–14 $\times 10^6$ g cm^{-3}. To truly assess the rate of these objects, a large volume-limited sample is needed.

8 CONCLUSION

We have modelled two transitional SNe Ia (SNe 2007on and 2011iv) using the abundance stratification technique. SNe 2007on and 2011iv both exploded in NGC 1404 at a distance modulus of 31.2 ± 0.2 mag. As well as being in the same galaxy, these SNe sit in an important area of parameter space. Understanding how they exploded will let us determine the connection between normal and sub-luminous SNe Ia. SN 2011iv was a low-energy (high ρ_c) Ch-mass explosion. It synthesized 0.31 M$_\odot$ ^{56}Ni, and had a $E_{\rm kin}$ of $1.2 \pm 0.3 \times 10^{51}$ erg. We favour a low-energy Ch-mass explosion model (W7e0.7), as it produces good spectral fits and provides results that are roughly consistent between the $E_{\rm kin}$ of the input density profile and the $E_{\rm kin}$ calculated from the integrated abundances. W7e0.7 is also the best-fitting density profile best suited to SN 1986G (another transitional SN Ia; Ashall et al. 2016). Our results are consistent with SN 2011iv being a delayed detonation Ch-mass explosion with a low $\rho_{\rm tr}$.

SN 2007on was less luminous than SN 2011iv but neither of them showed the Ti II absorption at maximum light, which is indicative of a sub-luminous SN Ia. The late-time spectra of SN 2007on show two separate components (see Mazzali et al. 2018). Therefore, we do not produce a 1-zone nebular model and 'complete' the abundance stratification experiment. Mazzali et al. (2018) demonstrate that these components could come from either the collision of two WDs, or a very off-centre ignition in the delayed detonation scenario. However, at early times, the two components are significantly below our photosphere, so the early-time results in this work are still valid.

[13] There could be an observer bias where only 1991bg-like SNe have been followed, as these were deemed more interesting.

Photospheric phase models were produced for SN 2007on using the W7, W7e0.7, and W7e2 density profiles. The W7 density profile produces marginally better fits, as the earlier fits from the W7e0.7 model were too hot, and those from W7e2 had too many high velocity lines.

If SN 2007on was a delayed detonation Ch-mass explosion, the fact that the W7 model produces the best fits indicates that it had a lower ρ_c than SN 2011iv. This agrees with the results of Gall et al. (2018). However, the lack of stable NSE elements (see Section 5.1 and Mazzali et al. 2018) in the ejecta of SN 2007on may favour the collision of two $\sim$0.7 M$_\odot$ WDs. Overall, as shown in Section 5.3, our spectral modelling results indicate that SNe 1986G; 2007on and 2011iv were consistent with being produced from a delayed detonation explosion, where SNe 1986G and 2007on had a similar $\rho_{\rm tr}$ but different ρ_c; and SNe 2011iv and 1986G had a similar ρ_c but different $\rho_{\rm tr}$.

To examine the area of transitional and sub-luminous SNe Ia further, we turned to previously published spectral models. SN 2004eo ($\Delta m_{15}(B) = 1.46$ mag) was proposed to be a standard delayed detonation Ch-mass explosion (Mazzali et al. 2008). SN 2003hv ($\Delta m_{15}(B) = 1.61$ mag) is compatible with either showed signs of a sub-Ch-mass detonation or a delayed detonation Ch-mass explosion, and SN 1991bg ($\Delta m_{15}(B) = 1.98$ mag) could have been a sub-Ch-mass detonation, a merger of two WDs, or a Ch-mass delayed detonation explosion. Either way, the diversity of SNe Ia at the faint end of the luminosity–width relation is large, and there are probably different explosion mechanisms, and possibly different progenitor channels, at work.

The introduction of the $s_{\rm BV}$ parameter has allowed fast declining SNe to become more standardizable (Burns et al. in preparation). It also provides a new parameter with which we can reaccess transitional SNe Ia. To do this, we computed the peak bolometric maximum ($L_{\rm max}$) for 24 SNe Ia, which were observed during the CSP. A large drop in the s_{BV} versus $L_{\rm max}$ relationship was found at $s_{BV} = \sim$0.5. Some have interpreted this as being an indication that there are two distinct populations of SNe Ia. However, we show that SN 1986G sits in this 'gap', and links sub-luminous and normal SNe Ia populations.

To explain the observational trend, we turn to the published models of Hoeflich et al. (2017). These models are delayed detonation Ch-mass explosions. To first order, the behaviour of SNe Ia, including that of the sub-luminous SNe Ia, can be explained by varying the $\rho_{\rm tr}$ in the explosion. The largest second-order effect for sub-luminous SNe Ia is the $\rho_{\rm c}$ of the WD. For normal SNe Ia, changes in $\rho_{\rm c}$ are insignificant. For example, a factor of 2 change will produce a change in ^{56}Ni mass of 10–20 per cent. For sub-luminous SNe Ia $\rho_{\rm c}$ has a large effect, due to most of the ^{56}Ni being produced in the deflagration phase. A factor of 2 change in $\rho_{\rm c}$ for the least luminous SNe will produce a factor of 2 change in ^{56}Ni mass. However, we note that just because the models fit almost all of the data does not mean that they are the only progenitor scenario we observe. There are hints, with supernovae such as SNe 2007on and 1991bg, of different progenitor and explosion channels, and it is likely that most progenitor scenarios do exist. However, currently the strongest evidence seems to suggest that the bulk of SNe Ia come from a one parameter family.

In conclusion, we find evidence that both SNe 2007on and 2011iv had ejecta masses similar to the Ch-mass and experienced a delayed detonation explosion. Although we note the possibility that SN 2007on could have originated from the collision of two similar mass WDs (e.g. Mazzali et al. 2018). Our overview of the faint end of the luminosity width relation has shown that there could be a smooth

continuum between normal and sub-luminous SNe Ia, which to the first order can be explained by varying ρ_{tr} in the delayed detonation explosion scenario. Looking forward to the future, we now have data sets where physical second-order effects can be examined. We need to explore the edges of the parameter space, with models (both abundance stratification and explosion) that produce less ^{56}Ni, and with models which explore alternative explosion scenarios more robustly. However, it appears that even at the faint end of SNe Ia distribution, most explosions come from Ch-mass objects.

ACKNOWLEDGEMENTS

C.A. would like to acknowledge support by the NSF research grant AST-1613472. M.D.S. acknowledges support by a research grant (13261) from VILLUM FONDEN. The work presented in this paper has been supported in part by NSF awards AST-1613472 (PI: E. Y. Hsiao), P. Hoeflich AST-1715133 (PI: P. Hoeflich), and AST-1613426 (PI: M. M. Phillips). We also acknowledge the Florida Space Grant Consortium. C.G. acknowledges support by the Carlsberg Foundation. The UCSC team is supported by NSF grant AST-1518052, the Gordon & Betty Moore Foundation, and from fellowships from the Alfred P. Sloan Foundation and the David and Lucile Packard Foundation to R.J.F. Support for programme #GO–12592 was provided by NASA through a grant from the Space Telescope Science Institute, which is operated by the Association of Universities for Research in Astronomy, Inc., under NASA contract NAS 5–26555.

REFERENCES

Arnett W. D., 1982, ApJ, 253, 785
Ashall C., Mazzali P., Bersier D., Hachinger S., Phillips M., Percival S., James P., Maguire K., 2014, MNRAS, 445, 4427
Ashall C., Mazzali P., Sasdelli M., Prentice S. J., 2016, MNRAS, 460, 3529
Ashall C., Mazzali P. A., Pian E., James P. A., 2016, MNRAS,
Ashall C. et al., 2017, preprint (arXiv:1702.04339)
Asplund M., Grevesse N., Sauval A. J., Scott P., 2009, ARA&A, 47, 481
Barna B., Szalai T., Kromer M., Kerzendorf W. E., Vinkó J., Silverman J. M., Marion G. H., Wheeler J. C., 2017, MNRAS, 471, 4865
Blondin S., Dessart L., Hillier D. J., Khokhlov A. M., 2017, MNRAS, 470, 157
Blondin S., Dessart L., Hillier D. J., 2018, MNRAS, 474, 3931
Bravo E., Domínguez I., Badenes C., Piersanti L., Straniero O., 2010, ApJ, 711, L66
Burns C. R. et al., 2011, AJ, 141, 19
Burns C. R. et al., 2014, ApJ, 789, 32
Cappellaro E., Mazzali P. A., Benetti S., Danziger I. J., Turatto M., della Valle M., Patat F., 1997, A&A, 328, 203
Dan M., Rosswog S., Brüggen M., Podsiadlowski P., 2014, MNRAS, 438, 14
Dan M., Guillochon J., Brüggen M., Ramirez-Ruiz E., Rosswog S., 2015, MNRAS, 454, 4411
Dessart L., Blondin S., Hillier D. J., Khokhlov A., 2014, MNRAS, 441, 532
Dhawan S., Leibundgut B., Spyromilio J., Blondin S., 2017, A&A, 602, A118
Diamond T. R., Hoeflich P., Gerardy C. L., 2015, ApJ, 806, 107
Dong S., Katz B., Kushnir D., Prieto J. L., 2015, MNRAS, 454, L61
Fang X., Thompson T. A., Hirata C. M., 2017, preprint (arXiv:1709.08682)
Fesen R. A., Milisavljevic D., 2016, ApJ, 818, 17
Fesen R. A., Höflich P. A., Hamilton A. J. S., Hammell M. C., Gerardy C. L., Khokhlov A. M., Wheeler J. C., 2007, ApJ, 658, 396
Fesen R. A., Weil K. E., Hamilton A. J. S., Höflich P. A., 2017, ApJ, 848, 130
Fitzpatrick E. L., 1999, PASP, 111, 63
Folatelli G. et al., 2012, ApJ, 745, 74
Frogel J. A., Gregory B., Kawara K., Laney D., Phillips M. M., Terndrup D., Vrba F., Whitford A. E., 1987, ApJ, 315, L129
Gall C. et al., 2018, A&A, preprint (arXiv:1707.03823)
Gamezo V. N., Khokhlov A. M., Oran E. S., Chtchelkanova A. Y., Rosenberg R. O., 2003, Science, 299, 77
Garnavich P. M. et al., 2004, ApJ, 613, 1120
Gerardy C. L. et al., 2007, ApJ, 661, 995
Goldstein D. A., Kasen D., 2018, ApJ, 852, L33
Hachinger S., Mazzali P. A., Tanaka M., Hillebrandt W., Benetti S., 2008, MNRAS, 389, 1087
Hachinger S., Mazzali P. A., Taubenberger S., Pakmor R., Hillebrandt W., 2009, MNRAS, 399, 1238
Hamuy M. et al., 1996, AJ, 112, 2408
Hoeflich P., Khokhlov A., 1996, ApJ, 457, 500
Hoeflich P., Khokhlov A. M., Wheeler J. C., 1995, ApJ, 444, 831
Hoeflich P., Khokhlov A., Wheeler J. C., Phillips M. M., Suntzeff N. B., Hamuy M., 1996, ApJ, 472, L81
Hoeflich P. et al., 2017, ApJ, 846, 58
Höflich P., 2003, Stellar Atmosphere Modeling, 288, 371
Höflich P., 2003, Stellar Atmosphere Modeling, 288, 185
Höflich P., Stein J., 2002, ApJ, 568, 779
Höflich P., Wheeler J. C., Thielemann F. K., 1998, ApJ, 495, 617
Höflich P., Gerardy C. L., Fesen R. A., Sakai S., 2002, ApJ, 568, 791
Höflich P., Gerardy C. L., Nomoto K., Motohara K., Fesen R. A., Maeda K., Ohkubo T., Tominaga N., 2004, ApJ, 617, 1258
Hristov B., Collins D. C., Hoeflich P., Weatherford C. A., Diamond T. R., 2017, preprint (arXiv:1711.11103)
Hsiao E. Y., Conley A., Howell D. A., Sullivan M., Pritchet C. J., Carlberg R. G., Nugent P. E., Phillips M. M., 2007, ApJ, 663, 1187
Hsiao E. Y. et al., 2015, A&A, 578, A9
Iben I., Jr, Tutukov A. V., 1984, ApJS, 54, 335
Iwamoto K., Brachwitz F., Nomoto K., Kishimoto N., Umeda H., Hix W. R., Thielemann F.-K., 1999, ApJS, 125, 439
Jiang J.-A. et al., 2017, Nature, 550, 80
Jordan G. C., IV, Perets H. B., Fisher R. T., van Rossum D. R., 2012, ApJ, 761, L23
Kepler S. O., Koester D., Romero A. D., Ourique G., Pelisoli I., 2017, 20th European White Dwarf Workshop, 509, 421
Khokhlov A. M., 1991, A&A, 245, 114
Khokhlov A. M., 1995, ApJ, 449, 695
Kushnir D., Katz B., Dong S., Livne E., Fernández R., 2013, ApJ, 778, L37
Leloudas G. et al., 2009, A&A, 505, 265
Lentz E. J., Baron E., Branch D., Hauschildt P. H., Nugent P. E., 2000, ApJ, 530, 966
Livne E., 1990, ApJ, 354, L53
Livne E., Arnett D., 1995, ApJ, 452, 62
Livne E., Asida S. M., Höflich P., 2005, ApJ, 632, 443
Lucy L. B., 1999, A&A, 345, 211
Maeda K., Röpke F. K., Fink M., Hillebrandt W., Travaglio C., Thielemann F.-K., 2010, ApJ, 712, 624
Maeda K. et al., 2010, Nature, 466, 82
Maund J. R. et al., 2010, ApJ, 725, L167
Mazzali P. A., 2000, A&A, 363, 705
Mazzali P. A., Hachinger S., 2012, MNRAS, 424, 2926
Mazzali P. A., Lucy L. B., 1993, A&A, 279, 447
Mazzali P. A., Podsiadlowski P., 2006, MNRAS, 369, L19
Mazzali P. A., Sauer D. N., 2008, MNRAS, 386, 1897
Mazzali P. A., Nomoto K., Cappellaro E., Nakamura T., Umeda H., Iwamoto K., 2001, ApJ, 547, 988
Mazzali P. A., Röpke F. K., Benetti S., Hillebrandt W., 2007, Science, 315, 825
Mazzali P. A., Maurer I., Stritzinger M., Taubenberger S., Benetti S., Hachinger S., 2011, MNRAS, 416, 881
Mazzali P. A. et al., 2014, MNRAS, 439, 1959

Mazzali P. A. et al., 2018, MNRAS, 476, 2905
Motohara K. et al., 2006, ApJ, 652, L101
Nomoto K., 1980, in Sugimoto D., Lamb D. Q., Schramm D., eds, IAU Symp. 93. Reidel, Dordrecht, p. 295
Nomoto K., Kondo Y., 1991, ApJ, 367, L19
Nomoto K., Thielemann F.-K., Yokoi K., 1984, ApJ, 286, 644
Nomoto K., Iwamoto K., Kishimoto N., 1997, Science, 276, 1378
Nugent P., Phillips M., 1995, ApJ, 455, L147
Pakmor R., Kromer M., Röpke F. K., Sim S. A., Ruiter A. J., Hillebrandt W., 2010, Nature, 463, 61
Patat F., Höflich P., Baade D., Maund J. R., Wang L., Wheeler J. C., 2012, A&A, 545, A7
Pauldrach A. W. A., Duschinger M., Mazzali P. A., Puls J., Lennon M., Miller D. L., 1996, A&A, 312, 525
Penney R., Hoeflich P., 2014, ApJ, 795, 84
Perlmutter S. et al., 1999, ApJ, 517, 565
Phillips M. M., 2012, PASA, 29, 434
Phillips M. M. et al., 1987, PASP, 99, 592
Phillips M. M., Lira P., Suntzeff N. B., Schommer R. A., Hamuy M., Maza J.é, 1999, AJ, 118, 1766
Piersanti L., Gagliardi S., Iben I., Jr, Tornambé A., 2003, ApJ, 583, 885
Pinto P. A., Eastman R. G., 2000, ApJ, 530, 744
Pinto P. A., Eastman R. G., 2000, ApJ, 530, 757
Prentice S. J. et al., 2017, preprint (arXiv:1709.03593)
Raskin C., Timmes F. X., Scannapieco E., Diehl S., Fryer C., 2009, MNRAS, 399, L156
Rasmussen C., Williams C., The MIT Press
Reinecke M., Hillebrandt W., Niemeyer J. C., 2002, A&A, 391, 1167
Remming I. S., Khokhlov A. M., 2014, ApJ, 794, 87
Rest A. et al., 2005, Nature, 438, 1132
Rheault J.-P., DePoy D. L., Behm T. W., Kylberg E. W., Cabral K., Allen R., Marshall J. L., 2010, Proc. SPIE Conf. Ser. Vol. 7735, Ground-based and Airborne Instrumentation for Astronomy III. SPIE, Bellingham, p. 773564
Riess A. G. et al., 1998, AJ, 116, 1009
Riess A. G. et al., 2016, ApJ, 826, 56
Röpke F. K., Hillebrandt W., Schmidt W., Niemeyer J. C., Blinnikov S. I., Mazzali P. A., 2007, ApJ, 668, 1132
Rosswog S., Kasen D., Guillochon J., Ramirez-Ruiz E., 2009, ApJ, 705, L128
Sasdelli M., Ishida E. E. O., Hillebrandt W., Ashall C., Mazzali P. A., Prentice S. J., 2016, MNRAS, 460, 373
Seitenzahl I. R. et al., 2013, MNRAS, 429, 1156
Sim S. A., Röpke F. K., Hillebrandt W., Kromer M., Pakmor R., Fink M., Ruiter A. J., Seitenzahl I. R., 2010, ApJ, 714, L52
Srivastav S., Anupama G. C., Sahu D. K., Ravikumar C. D., 2017, MNRAS, 466, 2436
Stehle M., Mazzali P. A., Benetti S., Hillebrandt W., 2005, MNRAS, 360, 1231
Stritzinger M., Leibundgut B., Walch S., Contardo G., 2006, A&A, 450, 241
Stritzinger M. D. et al., 2015, A&A, 573, A2
Stubbs C. W., Doherty P., Cramer C., Narayan G., Brown Y. J., Lykke K. R., Woodward J. T., Tonry J. L., 2010, ApJS, 191, 376
Tanaka M., Mazzali P. A., Stanishev V., Maurer I., Kerzendorf W. E., Nomoto K., 2011, MNRAS, 410, 1725
Timmes F. X., Brown E. F., Truran J. W., 2003, ApJ, 590, L83
Tripp R., 1998, A&A, 331, 815
Uenishi T., Nomoto K., Hachisu I., 2003, ApJ, 595, 1094
Walker E. S., Hachinger S., Mazzali P. A., Ellis R. S., Sullivan M., Gal Yam A., Howell D. A., 2012, MNRAS, 427, 103
Webbink R. F., 1984, ApJ, 277, 355
Weyant A., Wood-Vasey W. M., Allen L., Garnavich P. M., Jha S. W., Joyce R., Matheson T., 2014, ApJ, 784, 105
Whelan J., Iben I., Jr, 1973, ApJ, 186, 1007
Woosley S. E., Weaver T. A., 1994, ApJ, 423, 371
Woosley S. E., Kasen D., Blinnikov S., Sorokina E., 2007, ApJ, 662, 487
Yoon S.-C., Langer N., 2005, A&A, 435, 967
Zel'dovich Y. B., 1970, A&A, 5, 84
Zingale M., Woosley S. E., Rendleman C. A., Day M. S., Bell J. B., 2005, ApJ, 632, 1021

APPENDIX A: DISTANCE TO SN 2007ON AND SN 2011IV

The distance to NGC 1404 is very uncertain and could be anywhere between 13.6 and 27.9 Mpc. As SNe 2007on and 2011iv both exploded in this galaxy, we can use spectral modelling to quantify this distance. Fig. A1 contains spectral models of SN 2011iv and SN 2007on at −5.5 and −4.0 d relative to B-band maximum, produced for five different distance moduli. Here, as in the rest of this paper, we assume no host galaxy extinction. For a discussion on this, see Gall et al. (2018).

The models at the larger distance ($\mu = 31.6$ mag or $d = 20.9$ Mpc) do not produce good fits and are too hot. For example, the model of SN 2011iv has a very strong Si III λ4553 feature and too much flux in the near-UV. If the flux in the near-UV was reduced by adding metals to the outer layers of the ejecta, it would reprocess this flux into the optical and further increase the temperature and ionization state and would therefore worsen the fit. A poor fit can be seen in the SN 2007on model where the Si III λ4553 feature is too strong, and there is a weak Si (∼5970 and 6355 Å) ratio. Furthermore, the feature at 4900 Å at this epoch is dominated by Si II λλ5041 5056, but at this large distance the ionization state of Si is too high and there is not enough Si II absorption. Hence, it is apparent that the larger distance requires a luminosity (and therefore temperature) that is inconsistent with the observations.

The models at the shortest distance ($\mu = 30.8$ mag or $d = 14.5$ Mpc) also produce poor fits. For SN 2011iv, there is too much absorption in the UV. It also does not contain enough Fe III λ5156 absorption in the red side of the 4900 Å feature. Due to the lower distance and therefore luminosity and temperature, Fe II λλ5018, 5169 dominates this feature.

Therefore, a distance of $\mu = 31.6$ mag produces models that require a luminosity which is too high to match the observations, and a distance of $\mu = 30.8$ mag produces models that require a luminosity which is too low to match the observations. Hence, the optimum solution is somewhere in-between. The models at $\mu = 31.2$ mag produce the best fits. For SN 2011iv, the UV flux level is good, whilst the fit in the optical part of the spectrum has improved. For SN 2007on, the line shapes, depths, equivalent widths, and ratios are all remarkably good. Therefore, we adopt a distance modulus of $\mu = 31.0 \pm 0.2$ mag. More evidence of this distance is that it places SN 2007on and SN 2011iv on the correct part of the luminosity width relation.

APPENDIX B: LOG OF DATA

APPENDIX C: SNE IA BOLOMETRIC MAXIMUM DATA AND MODELS

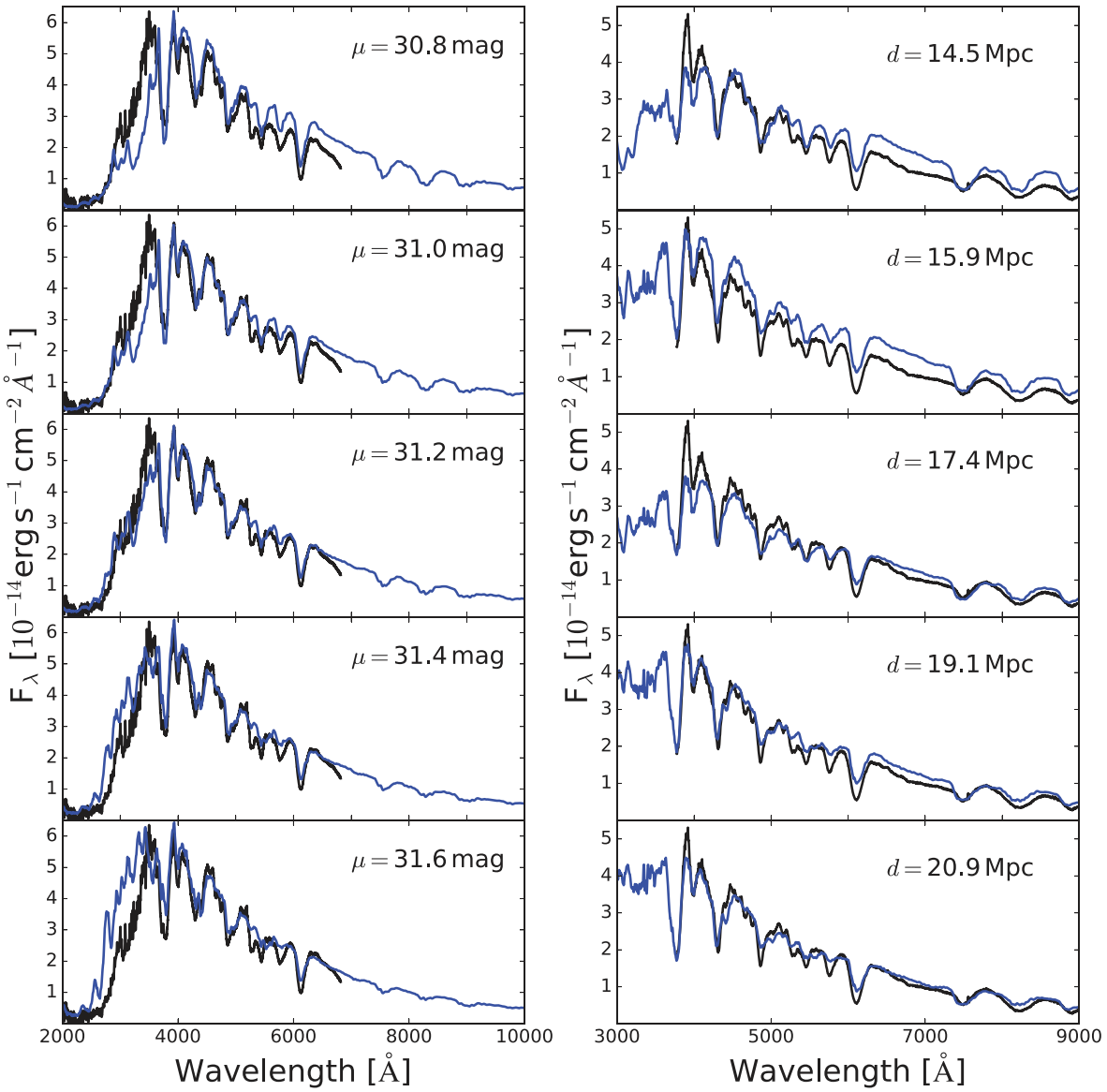

Figure A1. Spectra (black) and models (blue) of SN 2011iv (left) and SN 2007on (right) at –4.4 d and –4.0 d relative to *B*-band maximum. The models have been made for a range of distance moduli (i.e. 30.8 − 31.6 mag).

Table B1. The spectra of SN 2011iv.

Date	JD	Phase (days)[a]	Telescope	
4/12/2011	2455899.5	−6.6	du Pont	B&C
1/12/2011	2455901.0	−5.1	*Swift*	UVOT
5/12/2011	2455900.6	−5.5	du Pont	B&C
1/12/2011	2455902.1	−4.0	*Swift*	UVOT
1/12/2011	2455903.1	−3.0	*Swift*	UVOT
1/12/2011	2455905.1	−1.0	*Swift*	UVOT
11/12/2011	2455906.5	+0.4	*HST*	STIS
1/12/2011	2455907.2	+1.1	*Swift*	UVOT
11/12/2011	2455910.5	+4.4	*HST*	STIS
11/12/2011	2455915.5	+9.4	*HST*	STIS
11/12/2011	2455919.5	+13.4	*HST*	STIS
22/1/1987	2456166.8	+260.7	NTT	EFOSC

[a]Relative to *B*-band maximum in observer frame.

Table B2. The spectra of SN 2007on.

Date	JD	Phase (days)[a]	Telescope	
11/11/2007	2454415.8	−4.0	du Pont	WFCCD
14/11/2007	2454418.8	−1.0	du Pont	WFCCD
17/11/2007	2454421.7	+1.9	Baade	IMACS
19/11/2007	24554423.7	+3.9	NTT	EMMI
25/11/2007	24554429.7	+9.9	Clay	MagE

[a]Relative to *B*-band maximum in observer frame.

Table C1. The properties of the CSP SNe IA used in Fig. 10. The distance used to calculate the bolometric luminosity is indicated by asterisk (*). The different distance methods are: TF, Tully Fisher; SBF, Surface Brightness Fluctuation.

SN	L_{max} (10^{43} ergs^{-1})	z	Host velocity (km s^{-1})	LD (μ)[a]	$\Delta m_{15}(B)$[b] (mag)	$\Delta m_{15,s}(V)$[c]	s_{BV}[d]	Other μ (method)	Host galaxy
2005am	1.09 ± 0.08	0.0079	2368	32.94*	1.49	0.86	0.73	32.64 ± 0.80 (TF)	NGC 2811
2005el	1.20 ± 0.04	0.0149	4470	34.05*	1.36	0.58	0.84	...	NGC 1819
2005hc	1.59 ± 0.15	0.0459	13772	36.5*	0.83	0.61	1.19	...	MCG+00-06-003
2005iq	1.07 ± 0.06	0.0340	10206	35.8*	1.25	0.83	0.87	...	eso538G013
2005ke	0.27 ± 0.02	0.0049	1463	31.43	1.69	1.27	0.42	31.89 ± 0.84 (TF)*	NGC 1371
2006D	1.27 ± 0.06	0.0085	2556	33.10*	1.36	0.87	0.81	...	MCG -01-33-34
2006bh	1.01 ± 0.05	0.0108	3253	33.28*	1.41	0.82	0.80	33.22 ± 0.1 (TF)	NGC 7329
2006et	1.79 ± 0.11	0.0226	6787	34.87*	0.84	0.55	1.09	...	NGC 0232
2006gt	0.67 ± 0.05	0.0448	13422	36.43*	1.64	1.10	0.56	...	[e]
2006mr	0.15 ± 0.03	0.0059	1760	31.87	1.93	1.42	0.25	31.25 ± 0.51(TF,SBF)*	NGC 1316
2007N	0.17 ± 0.02	0.0129	3861	33.91*	2.12	1.32	0.30	34.06 ± 0.18 (TF)	MGC0133012
2009F	0.22 ± 0.02	0.0130	3884	33.74*	1.97	1.37	0.33	...	NGC 1725
2007af	1.18 ± 0.07	0.0055	1638	32.16	1.19	0.62	0.93	31.75 ± 0.05 (Cephid)*	NGC 5584
2007ba	0.67 ± 0.02	0.0385	11546	36.18*	1.67	1.37[f]	0.55	...	UGC 09798
2007bd	1.24 ± 0.06	0.0309	9266	35.73*	1.24	0.72	0.88	...	UGC 04455
2007hj	0.63 ± 0.05	0.0141	4231	33.73*	1.63	1.02	0.60	...	NGC 7461
2007le	1.14 ± 0.06	0.0067	2015	31.88	0.93	0.63	1.02	...	NGC 7721
2007on	0.73 ± 0.04	0.0065	1947	32.13	1.96	1.11	0.57	31.2 ([g]+this paper)*	NGC 1404
2009aa	1.43 ± 0.07	0.0273	8187	35.48*	1.21	0.69	0.91	-	ESO57G020
2008fp	2.05 ± 0.20	0.0056	1698	32.16	0.76	0.64	1.08	31.82 ± 0.01[h]*	ESO 428-G14
2008hv	1.20 ± 0.04	0.0125	3762	33.85*	1.31	0.76	0.85	...	NGC 2765
2008ia	1.19 ± 0.10	0.0219	6578	34.96*	1.23	0.75	0.84	...	ESO125006
2009Y	1.86 ± 0.16	0.0094	2804	33.20*	0.97	0.70	1.19	32.20 ± 0.27 (TF)	NGC 5728
2009ag	1.13 ± 0.10	0.0086	2590	33.01*	1.05	0.80[c]	0.96	32.18 ± 0.3 (TF)	ESO 492-2

[a] Luminosity distance corrected to the reference frame defined by the 3K microwave background radiation.
[b] Obtained from SNOOPY.
[c] Obtained from Hoeflich et al. (2017).
[d] Obtained from Burns et al. (2014).
[e] 2MASXJ00561810-0137327.
[f] This value is uncertain due to poor temporal coverage.
[g] Gall et al. (2018).
[h] Weyant et al. (2014).

Table C2. Delayed detonation models from Hoeflich et al. (2017).

Model	$log(L_{max})$	s_{BV}	ρ_{tr}	ρ_c
	erg s^{-1}		10^7 g cm^{-3}	10^9 g cm^{-3}
8	42.21	0.33–0.60	8	2
8r1	42.54	0.31–0.55	8	1
8r2	42.70	0.29–0.53	8	0.5
10	42.49	0.40–0.60	10	2
12	42.57	0.44–0.63	12	2
14	42.69	0.47–0.63	14	2
16	42.84	0.50–0.67	16	2
16r1	42.90	0.48–0.65	16	1
16r2	42.91	0.46–0.64	16	0.5
18	42.98	0.57–0.69	18	2
20	43.06	0.64–0.70	20	2
23	43.17	0.78–0.86	23	2
23d1	43.20	0.78–0.90	23	0.5
23d2	43.19	0.78–0.88	23	1.1
25	43.22	0.92–1.02	25	2
27	43.25	0.99–1.08	27	2
HeD6	42.89	1.00–1.60	n/a	0.01
HeD10	43.35	0.80–1.10	n/a	0.03

This paper has been typeset from a TEX/LATEX file prepared by the author.